Assessing the riveting process and the quality of riveted joints in aerospace and other applications

Chapter · October 2017

1 author:

Gang Li
National Research Council Canada
68 PUBLICATIONS   **541** CITATIONS

SEE PROFILE

Some of the authors of this publication are also working on these related projects:

Composite structures View project

composite joints View project

Chapter 6   Assessing the riveting process and the quality of riveted joints in aerospace and other applications

Gang Li[*], Guoqin Shi, and Nicholas C Bellinger

Structures and Materials Performance Laboratory, Institute for Aerospace Research
National Research Council Canada, 1200 Montreal Road, Ottawa, ON, Canada K1A 0R6

Abstract: This chapter first reviews several aspects of the riveting process to ensure that riveted joints will have excellent fatigue performance. These aspects include solid rivets, joint design rules, several experimental and numerical methods to determine the residual stress/strain and interference in riveted joints, and the current approach for studying the riveting process. It then provides two case studies using experimental and finite element methods to explore (i) the effect of the riveting process on the residual stress/strain in joints, and (ii) the stress condition in riveted lap joints when the joints are remotely loaded in tension. Concluding remarks on the potential development direction of the riveting tools and rivets are briefly provided.

Keywords: residual stress/strain; rivet squeeze force; joint; riveting; finite element

6.1   Introduction

The following sections are covered in the chapter to study the riveting process and its effect on riveted lap joints. Section 6.1 is the content outline of the chapter. Section 6.2 reviews the riveting process and quality assessment of the rivet installation. This review section includes solid rivets, joint design rules, and joint quality assessment. Section 6.3 reviews several experimental and numerical methods to determine the residual stress/strain and interference induced by the riveting process. Section 6.4 is the review summary and recommendations for the riveting process research. Section 6.5 provides two case studies using experimental and finite element methods. Case study 1 studies the effect of the riveting process on the residual stress/strain and interference, and case study 2 studied the stress condition in the riveted lap joints during the joint tensile loading stage. Section 6.6 provides brief concluding remarks on potential development trends of riveting tools and rivets aimed at greater fatigue performance in riveted lap joints. Acknowledgements and references are then provided. The main objective of this chapter is to identify and justify the recommended feasible and reliable research approaches for an accurate study of the stress/strain condition in the riveted lap joints, from the riveting process to the joint tensile loading stage. The obtained knowledge can be used to (i) identify weak locations in a joint, (ii) ensure that the riveted joints has great fatigue

---

[*] Corresponding author, PhD, Research Officer, Tel. (613)990-4989, Fax: (613)998-8609, E-mail: Gang.Li@nrc-cnrc.gc.ca.

performance, (iii) accurately assess joint fatigue life, and (iv) improve the fatigue life by developing new riveting tools and rivets.

6.2 Riveting process and quality assessment of the rivet installation

6.2.1 Solid rivets

Solid rivets are one-piece fasteners consisting of a smooth cylindrical shaft with a head on one end, which are installed by mechanically upsetting on the shaft tail side. Solid rivets can have flush or protruding heads. These two types of solid rivets are extensively used in aircraft structures.[1] Flush head rivets are also called countersunk head rivets. The protruding head rivets include brazier head, flat head, round head, and universal head rivets, as shown in Fig. 6.1. Countersunk head rivets are used where high aerodynamic efficiency is required, for instance, at longitudinal lap joints in a fuselage. Brazier head rivets can be used on external surfaces of noncombat aircrafts. Other protruding head rivets, like round and flat head rivets, are used on internal structures based on major factors of integrity and/or aerodynamic efficiency requirements. Protruding head rivets can be replaced by universal head rivets.

Typical materials for aircraft rivets include aluminium alloys, titanium, and nickel based alloys. The aluminium alloys are usually 1100, 2017, 2024, 2117, 7050, 5056, and V-65. Markings on the manufactured rivet head, such as small raised or depressed dimples, raised cross, raised dot, raised double dash, or raised ring, indicate the rivet's material, as shown in Table 6.1. The material code is used to identify the rivet material. Rivet diameters are measured in 1/32 inch (25.4/812.8 mm) increments and lengths in 1/16 inch (25.4/406.4 mm) increments. The shank diameter and rivet length are labelled after the material code in the rivet designation. As an example, the rivet designation of a 100° countersunk head rivet is presented in Fig. 6.2 where "MS" stands for "Military Standard specification". Similarly, "AN", if used to replace "MS", stands for "Air Force/Navy Standards specification", and "NAS" for "National Aerospace Standard specification". The rivet type number "20426" refers to a 100° countersunk head rivet; material code "AD" refers to the 2117-T4 aluminium alloy material for the rivet, the rivet shank diameter is 4/32″ (101.6/812.8 mm), and the rivet length is 5/16″ (127/406.4 mm).

The installation of these solid fasteners requires access to both sides of the riveted structures. Solid rivets are driven using a hydraulically, pneumatically, or electromagnetically driven squeezing tool. A riveted joint using the same rivets is the most efficient, since all the rivets could reach capacity simultaneously.
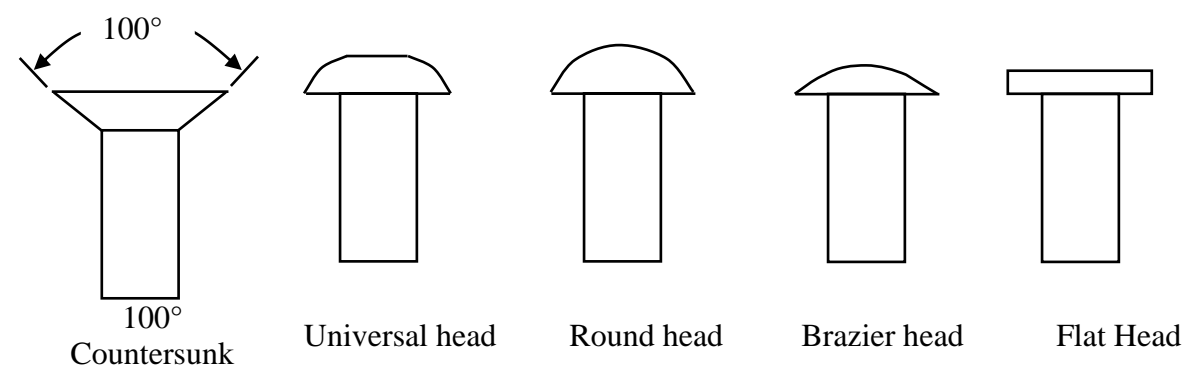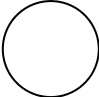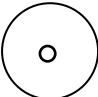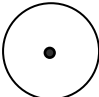
100°	Universal head	Round head	Brazier head	Flat Head
100° Countersunk				
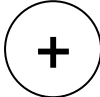
Fig. 6.1 Solid rivet head shapes.

Table 6.1 Some rivets information.[1-4]

Material	Aluminium	Aluminium alloy			
	1100-F	2117-T4	2017-T4	2024-T4	5056-H32
Material code	A	AD	D	DD	B
Markings	Plain	Dimple	Raised dot	Raised double dash	Raised cross

MS20426AD4-5

"MS" refers to the used standard

"20426" refers to the rivet type (100° flush head)

"AD" refers to the 2117-T4 aluminium alloy material

"4" refers to the 4/32″ rivet shank diameter

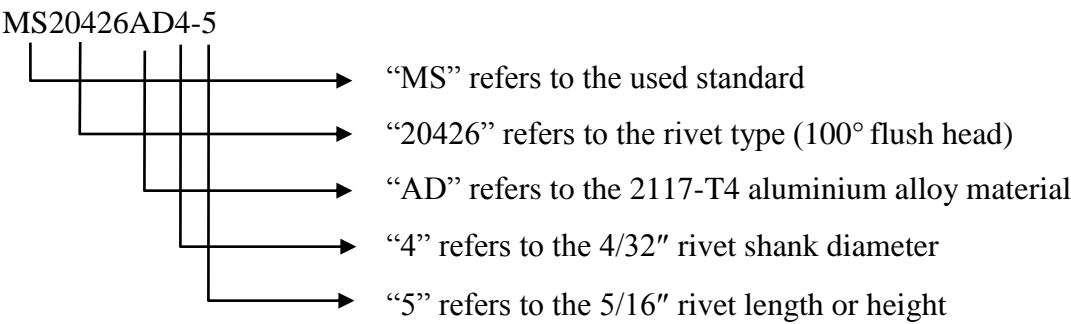"5" refers to the 5/16″ rivet length or height

Fig. 6.2 A rivet designation.

6.2.2   Preparations of riveting process and quality assessment

Several factors are assessed to identify the suitable solid rivets for joints. These factors include the aerodynamic efficiency, the sheet material and thickness, the rivet strength, the rivet type including shank diameter and height, the joint working requirements, etc. Some design rules for good fatigue life capability can be summarized as:[1-4] (i) the rivet spacing should be 4 rivet shank diameters or more; (ii) the minimum edge margin should be at least two rivet shank diameters; (iii) the rivet shank diameter should be equal or greater than three sheet thicknesses; (iv) before riveting, the rivet height out of the other sheet surface should be 1.5 rivet shank diameters; (v) the hole should be 3 to 6 thousandths of an inch greater than the rivet shank diameter; (vi) for flush head rivets, the countersunk depth should not penetrate the entire outer sheet thickness and/or the sheet thickness should be at least 1.5 the countersunk depths; (vii) the recommended maximum driven head diameter should be within the range of 1.3 to 1.8 shank diameters; usually, a 1.5 shank diameters is suggested; and (viii) the driven head height beyond the sheet surface should be 0.3 shank diameters or more.

Good hole filling and hole expansion are important to achieve high fatigue resistance of the joint holes and a high yield stress of the rivet is preferred. After riveting, rivets fill the hole completely to establish an interference fit at the hole edge region. To avoid the defects introduced into rivets during the riveting process, the rivet driven head deformation should not be beyond the rivet material deformation limits to avoid cracking in the rivets. The riveted joint structures must be inspected visually to ensure good rivet installations. Unacceptable defects must be identified based on related specifications[1, 2] and should be discarded. The defects can include poorly filled holes, titled rivets (usually cannot be beyond 2 degrees[5]), loose rivets, cracks in rivet flush and driven heads, bulging skin, etc.

6.3 Determination of residual strains and interference in riveted lap joints

Due to plastic deformation, the total elastic deformation energy cannot be completely released after the riveting process. Thus, interference and compressive residual stresses and strains are created at the hole edge region. The residual stresses and strains, as well as the interference, have a significant effect on the joint fatigue behavior. [1-16] Because of the complexity associated with the joint riveting process, there are no accurate theoretical solutions to handle the three dimensional residual stress and strain fields in the vicinity of the hole. Experimental and finite element (FE) methods are usually adopted to estimate the induced residual stress/strain condition and interference.[4, 7-28]

6.3.1   Experimental measurements

Several methods can be used to measure residual strains.[4, 9, 10, 17, 18, 21-28]   The corresponding residual stresses are then determined using the measured strains. These methods include strain gauge, neutron diffraction, X-ray diffraction, ultrasonic, optical, magnetic method based on

Barkhausen noise, local melting, and partially destructive technique like drilling holes. Several measurement methods are briefly summarized in the following.

Entire in-situ strain variations in both the radial and hoop (tangential) directions, during the riveting process, at specific surface positions, can be measured using micro-strain gauges.[21-28] Gauges, mounted on some area experiencing large deformations, will be damaged if the actual strains are greater than the gauges' strain limits. Residual strains in the hole vicinity and inside the panels cannot be measured using this method. The measured strains are average values over the strain gauge area. This method is convenient, reliable, economical, and non-destructive.

Neutrons can penetrate through many centimeters of aluminum alloy sheets, but X-rays cannot penetrate deeply into sheets.[10, 26] Thus, the neutron diffraction technique and X-ray can measure residual strains inside the material, which is superior to the strain gauge method. Both methods are non-destructive. Stress/strain free (unriveted open hole) coupons are used as references to estimate the residual strains in the tested/riveted coupons. The provided strains are the average values of each measured gauge volume. The gauge volume is determined by material properties, grain size, statistical quality, spatial resolution of the instrument, experienced staffs, etc.

The ultrasonic method is based on the well established behavior of echo signal amplitudes,[9] which are a function of interference or residual strain. The ultrasonic method is non-destructive. However, to establish the correlation between the interference or residual strain and an ultrasonic signal amplitude, destructive actions have to be carried out on other coupons riveted at the same conditions to get the hole edge expansion data. The measured amplitude obtained using an open hole coupon results in the zero interference fit signal.

Photoelastic stress measurements, rivet-sheet springback measurements, and micro-hardness measurements are also used to measure the residual stress at the faying surface in riveted lap joints. However, as pointed out by Müller[4] in 1995 experimental techniques for the direct measurement of residual stresses are far from simple.

6.3.2   Finite element methods

Finite element (FE) methods are powerful tools that are used to simulate many problems, including the study of residual stresses/strains in riveted joints since the 1990's. Initially, some researchers [11, 12, 19] used simplified methods to introduce the assumed interference fit in riveted lap joints. These simplified methods include the misfit method, thermal expansion method, and rivet squeeze force method. With these methods, variations in the assumed residual stresses/strains and interference through the hole thickness direction cannot be accurately introduced. For the misfit method, the radial and clamping interference stresses are generated by forcing radial and rivet height conformity between the initially oversized ratio of rivet shank over the sheet hole dimension, and the undersized ratio of the shank height

value over the package depth of the two joint sheets. For the thermal expansion method, the rivet shank is given orthotropic properties with different coefficients of thermal expansion in the shank axial and lateral directions. The temperature of the rivet shank is changed to reduce its length and to expand it in the radial direction. Thus, the two sheets are gripped by the rivet and initial interference stresses are generated.[11, 12] For the squeeze force method, the squeeze force is directly applied and maintained at the top and bottom of each rivet. The drive head shape of these rivets is assumed. Stresses/strains generated in the joints are treated as residual stresses/strains. Following the use of these three methods, the effect of the residual stress/strain can be further qualitatively analyzed by applying a joint remote tensile load.[11, 12, 19]

Current FE models can analyze the complicated riveting process either using the displacement- or the force-controlled riveting methods. Nonlinearities in material behaviour, structural geometry, and contact boundary conditions can be taken into account. For the displacement- or force-controlled riveting process, two load steps are needed. One step is to use displacements or forces to control the rigid pusher to squeeze the rivet, and the second step is to move the pusher back and away from the rivet. The created stresses and strains in the riveted joint are the residual stresses and strains. Rivet driven head shapes are determined by the applied compressive displacement or rivet squeeze force, and are therefore not assumed as in the above simplified methods.

Some researchers used velocity to control the rivet installation.[21, 22] The squeezing velocity was 2 mm/minute during the testing and 10 m/second was used for the three-dimensional (3D) FE analysis. A countersunk 7050 aluminum alloy rivet, with a 4 mm shank diameter, was used along with two 2024-T351aluminum sheets, 1.6 mm thick. The researches found that inertia and wave propagation effects were limited if the crushing velocity was on the order of 10 m/second. Ryan and Monaghan[14] in 2000 used an elastoplastic two-dimensional (2D) axisymmetric FE model to simulate the residual stress fields for both fiber metal laminate and typical aluminum alloy riveted countersunk joints. One rigid die was stationary and the other rigid pusher moved at a constant velocity of 17 mm/second. The sheet materials were 2024-T3 aluminum alloy. Fiber metal laminates were made of two aluminum layers, with a layer of glass fiber in between. The rivet was made from 2117-T3 aluminum alloy.

A large number of aircraft manufacturers use rivet-tail shape parameters, such as tail height and tail diameters, as a means to assess the quality of the riveted joints. Rivets are usually installed using displacement-controlled, which results in an unknown rivet squeeze force. Thus, the relation between the rivet squeeze force and the induced residual stresses/strains and/or interference cannot be identified. To establish this relation and provide the necessary knowledge to enhance the joint fatigue life, force-controlled riveting method is superior to the displacement-controlled riveting method. A 2D axisymmetric FE model can be employed.[4, 15, 23-28] After the rivet squeeze force is removed, the residual stress/strain and interference,

induced by the riveting process, can then be analyzed by extracting the corresponding data at specific locations from the FE model. Because the finite element model needs only a one-quarter joint geometry, a very fine mesh can be used at the high stress areas. A 2D axisymmetric FE model usually has three deformable contact bodies, two circular sheets and one rivet, and two rigid contact surfaces, one stationary at the rivet flush head side and a rigid pusher contacting the rivet tail. To eliminate edge effects, the sheet should extend approximately 5 rivet shank diameters from the axis of symmetry. It has been found from these FE results that an increasing maximum squeeze force not only pushes the zone of tensile hoop stress away from the hole periphery, but also results in a larger driven head size. The relation between the rivet driven head deformation and squeeze force can be identified, interference magnitude and variation through thickness can be determined at each specific squeeze force, and full-field contours for both the residual stresses and strains can be provided. However, the 2D axisymmeteric FE model cannot simulate the final stress conditions when joints are in tension. A 3D FE model is required for this situation.

6.4 Summary and recommendations for the riveting process research

An order of 2% to 3% interference fit should be enough to ensure that a joint is waterproof and has a prolong service life.[7] The compressive residual hoop stresses in the area near the hole periphery can greatly retard crack nucleation, as well as slow the growth of a crack in its early stage. Experimental results showed that fatigue life increases with larger squeeze forces, and decreases with an increase in fatigue load.[15] Due to the large nonlinear variation through the joint thickness, there can be large differences present in the interference fit and residual stress between the inner and outer sheets.[25, 26] For instance, large interference and residual stresses are created in the inner sheet neighboring the rivet drive head side. On the other hand, the corresponding interference and residual stresses are very small in the joint outer sheet. Accurate understanding of the magnitude and variation of the interference fit and residual stresses/strains is critical to achieve a better understanding of the joint fatigue life. To achieve this goal, which will help improve the riveted joint fatigue performance, accurate FE models are required. Currently, there are no theoretical solutions for the complicated 3D residual stress/strain induced by the riveting process. Thus, experimental and FE methods are usually adopted. Experimental data are used to validate the FE models, and the validated FE models are then further used to carry out parametric studies. A force-controlled riveting method in the FE methods, combined with the necessary experimental testing, is highly recommended. A quasi-static force-controlled riveting method offers a better control of the rivet installation, and provides the consistent conditions at and around the rivet/sheet hole interface in the riveted lap joints.[4, 6, 15] Accurate elastoplastic stress-strain curves of the joint materials are required for a good finite element analysis. Experimental data like the measured residual strains, driven head deformations, and/or interference are needed to validate the finite element results at specific squeeze force levels. Two-dimensional axisymmetric FE methods are only appropriate to study the riveting process.[4, 15, 23, 25, 26] When the joints are remotely loaded in

tension, the final stress condition in the joints, considering the effects of the squeeze force and other factors, can be studied using 3D FE methods.[27, 28] For clarity, two case studies are provided in the following section.

6.5 Case study using the force-controlled riveting method

Case studies 1 and 2 will address two issues, (i) the effect of the riveting process and (ii) the stress condition during the joint tensile loading stage. Joints riveted using the countersunk head rivets of the MS20426x-x type are studied.

6.5.1 Case study 1: effect of the riveting process on residual stress/strain in joints

A two stage approach was used; 1) validate the 2D axisymmetric FE method using corresponding experimental data, and 2) study the effect of squeeze force on the residual stress/strain using the validated 2D axisymmetric FE model.[25, 26] For the first stage, three joint specimens were fabricated, one with micro-strain-gauges and the other with no gauges. The assembly process used a 53.38 kN squeeze force. Micro-strain gauges and neutron diffraction were used to determine the strain variations in the joint during and after the riveting process. The experimental strain data and rivet driven head deformations were used to verify the numerical model. In the second stage, six additional unstrain-gauged joints, two joints at each squeeze force level, were riveted using the rivet squeeze forces of 26.69 kN, 35.59 kN, and 44.48 kN. Only the rivet driven head deformations were used to validate the corresponding FE results. The residual stress/strain conditions at any position within the lap joint, as well as the full-field stress and strain contours, can be extracted from the validated FE results. Details can be found elsewhere[25, 26] and some information is provided in this chapter.

Joint and materials

The specimen configuration used in this study is shown in Fig. 6.3 and consisted of two 76.20×76.20 mm bare 2024-T3 Al alloy sheets, each 2.03 mm thick, and one 2117-T4 Al alloy 100° countersunk type rivet MS20426AD8-9. The material properties used for the bare sheets were $E = 72.4$ GPa, $v = 0.33$, and $\sigma_y = 310$ MPa (initial yield stress), whereas those used for the 2117-T4 Al alloy rivet[15] were $E = 71.7$ GPa, $v = 0.33$, and $\sigma_y = 172$ MPa. The rivet had a total length of 14.29 mm and shank diameter, D, of 6.35 mm. The mean inner sheet hole diameter was 6.45 mm and the rivet mean protruding height above the inner sheet surface was 9.95 mm based on the optical measurement results of 20 specimens. An isotropic hardening behavior was assumed for both the sheet and rivet materials. When the true stress was beyond the initial yield stress, the material constants C and m were determined using the curve fitting method by substituting the uniaxial tensile test data [24] into Eq. [6.1]:

$$\sigma_{true} = C(\varepsilon_{true})^m \tag{6.1}$$

where σ_{true} is the true stress, ε_{true} is the true strain. The hardening parameters used for the 2.03 mm thick sheet were: $C = 765.67$ MPa and $m = 0.14$ when $\varepsilon_y < \varepsilon_{true} \leq 0.02$ (ε_y was the initial yield strain), $C = 744.62$ MPa and $m = 0.164$ when $0.02 < \varepsilon_{true} \leq 0.10$, and the slope of the linear hardening curve was 1.034 GPa when $\varepsilon_{true} > 0.10$. The hardening parameters[15] used for the rivet were: $C = 544$ MPa and $m = 0.23$ when $0.02 < \varepsilon_{true} \leq 0.10$, and $C = 551$ MPa and $m = 0.15$ when $0.10 < \varepsilon_{true} \leq 1.0$.

In order to avoid both the thermal and inertial influence on the specimen, a small constant loading ramp of 111.2 N/second was chosen for the force-controlled riveting,[24] which is very slow compared to the actual rivet loading rates.
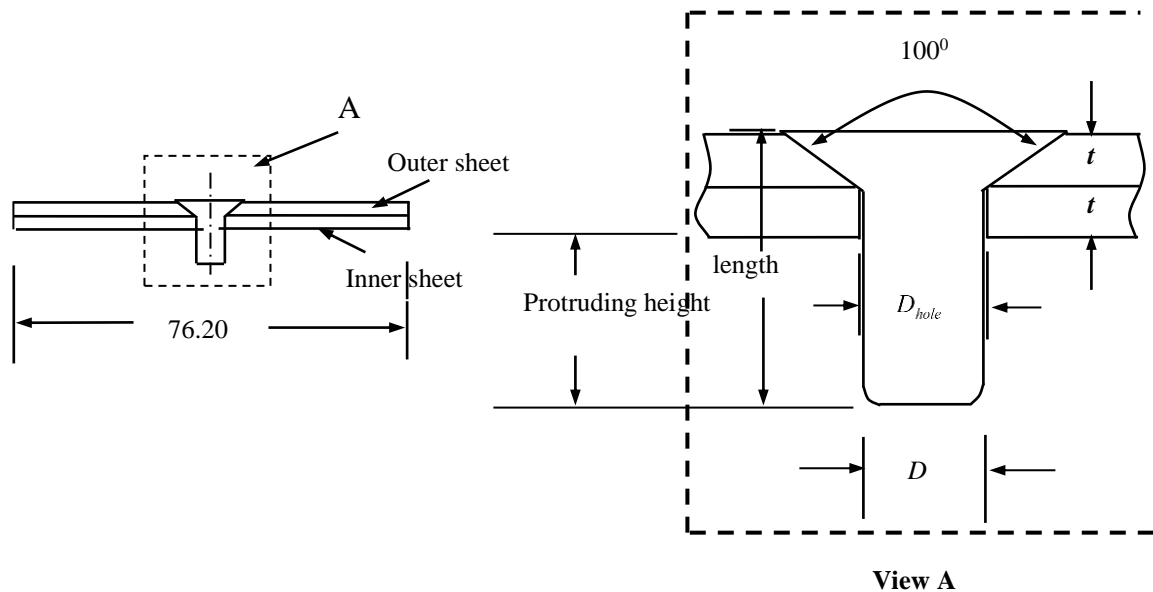
Fig. 6.3 Specimen geometry (dimensions: mm).

After riveting, one riveted and one unriveted specimen (strain/stress free joint) were sent to the Chalk River Laboratory of the Steacie Institute for Molecular Science, National Research Council Canada, to measure the residual strains in the riveted lap joint using neutron diffraction. Since neutrons penetrate many centimeters through aluminum alloys, neutron diffraction has been used as a non-destructive technique to measure the internal strains present in aluminum components.

Measurements

In-situ measurements of the strain variation in both the radial and hoop (tangential) directions were obtained during the riveting process using the micro-strain gauges. Fig. 6.4 shows the

micro-strain gauge arrangement on the joint inner sheet surface. By defining the radial coordinate value of r to be zero at the joint hole centre, the strain gauge locations can be identified. Gauges R1 to R4 were located at r = 7.85 mm, 10.55 mm, 13.35 mm, and 16.15 mm, while Gauges H1 to H4 were at positions r = 7.88 mm, 10.35 mm, 12.86 mm, and 15.38 mm. Gauges R1 to R4 (Micro-Measurements EA-13-031EC-350 with gauge factor of 2.09±1.0%) were used to measure the radial strain values and gauges H1 to H4 (Micro-Measurements EA-13-031DE-350 with gauge factor of 2.06±1.0%) were used to measure the hoop direction strain values.

By aligning the specimen in the proper direction, three normal strains, at specific locations inside the sheets, can be determined using the neutron diffraction technique. The three normal stresses can be estimated from these three strain components. The goal was to obtain data close to the rivet/sheet and sheet/sheet interfaces using the neutron diffraction technique. However, the fine spatial resolution required a small instrumental gauge volume. Aluminum sheet has a relatively small coherent cross section for neutron measurements, imposing a lower limit of approximately 1 mm^3 on the gauge volume to obtain data of sufficient statistical quality. Two gauge geometries were therefore required. For the measurements of the x and y components of strain, the gauge dimensions were 0.5×0.5×5 mm with the 5 mm dimension parallel to z and a diamond cross-section in the x-y plane. For the z (hoop) component, the dimensions were 1×1×1 mm with a rectangular cross section in the x-z plane. Setup of riveted lap joint using neutron diffraction measurement is shown in Fig. 6.5. The neutron diffraction measurement locations were relatively far from the sheet surface for accuracy reason.
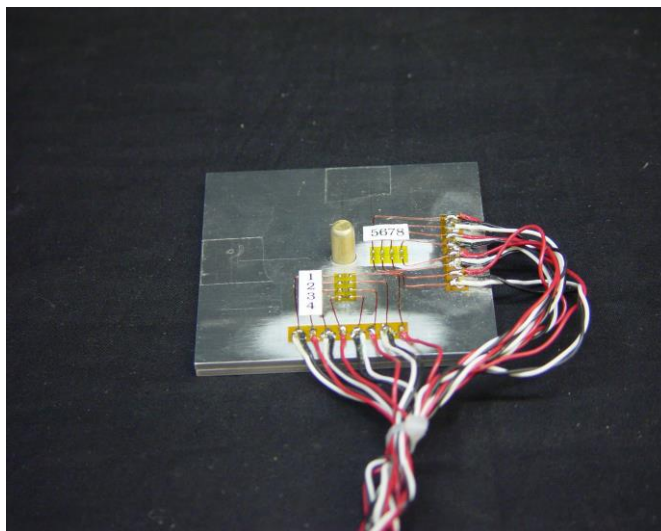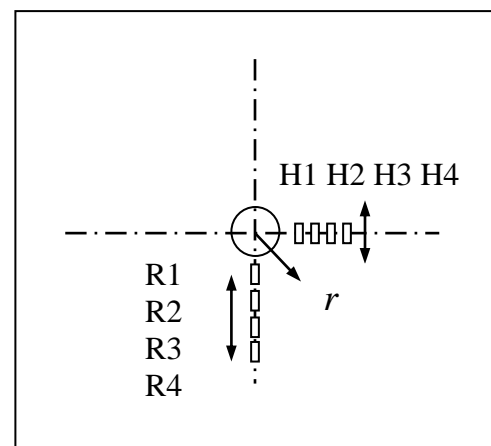
(a)   (b)

Fig. 6.4 Micro-strain gauge arrangement on the inner sheet surface before riveting for (a) an experimental coupon set-up, and (b) a schematic representation.
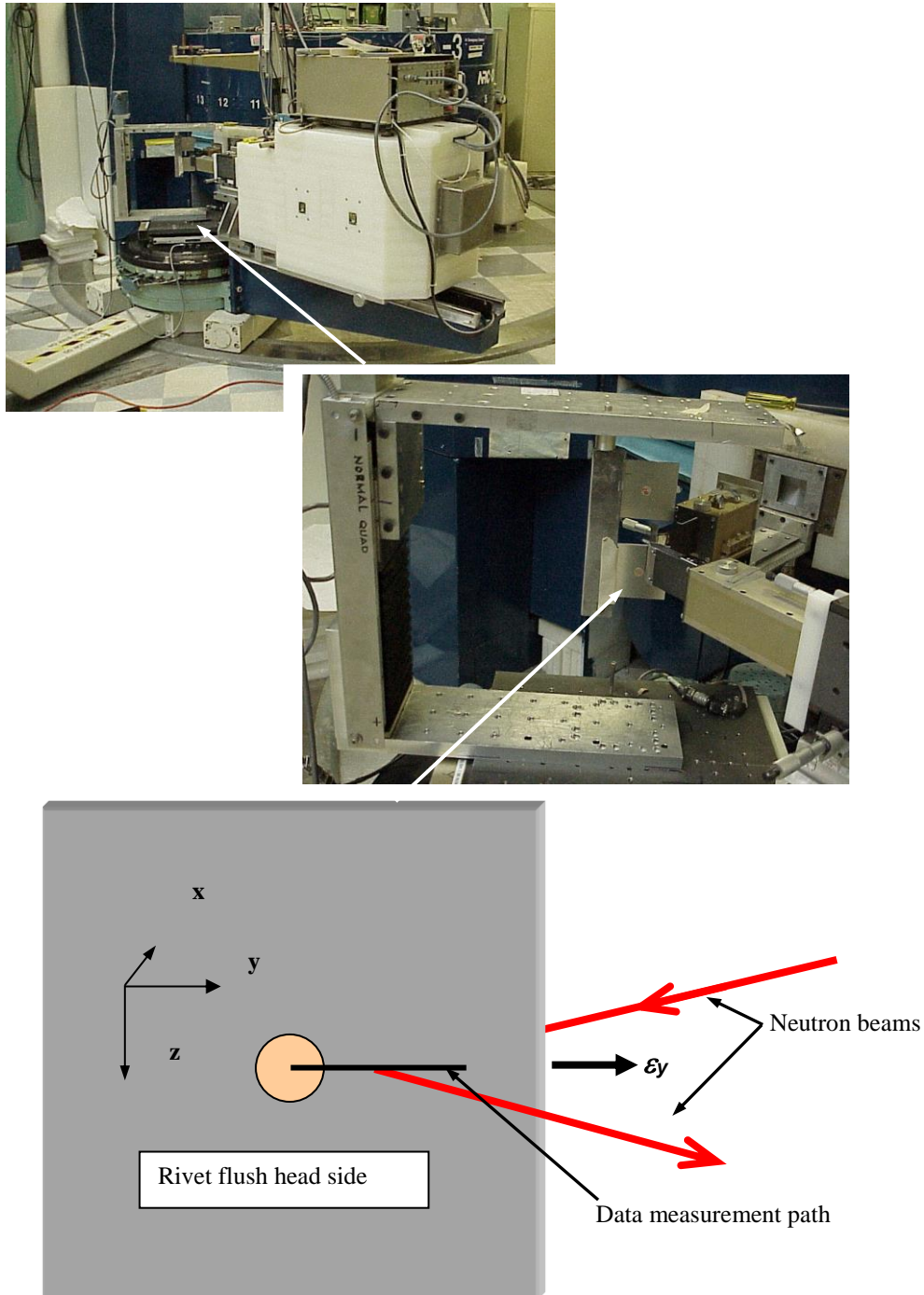
Fig. 6.5 Setup of riveted lap joint for neutron diffraction measurement.

Numerical simulation

A 2D axisymmetric FE model, using MSC.Patran (pre- and post-processor) version 2001r1 and MSC.Marc (solver) version 2001, was developed to study the riveting process.[25, 26] Material and geometry non-linear properties, as well as the contact situations, were considered in the numerical simulations. Different mesh sizes were examined to determine the convergence of the rivet deformation and the maximum rivet shank diameter deformation ratio of $\dfrac{D_{max}}{D}$, where D is the rivet shank diameter before riveting and D_{max} is the maximum rivet shank diameter after riveting. A very fine mesh was chosen with a total of 5410 nodes and 5099 4-node axisymmetric elements with reduced integration. The mesh for the sheets extended to 5 rivet shank diameters ($5D$) from the joint symmetric axis, **x**, as shown in Fig. 6.6. The squeeze force was applied to the rigid pusher, which compressed the rivet driven head edge. A coefficient of friction of 0.2 was used in the Coulomb model.[15, 25-28] A tabular listing of the stress and plastic strain values were entered into a table provided by the MSC.Patran interface, which used linear interpolation for values between the points to implement the hardening behavior of the model. Isotropic hardening behavior was assumed for both the rivet and sheet materials.

During the riveting process, the contact areas are (i) the faying surface between the inner and outer sheets, (ii) the area between the inner sheet and rivets, (iii) the area between the outer sheet and rivets, (iv) the area between the rivets' driven heads and the rigid pushers, and (v) the area between the rivets and the rigid supporting surface. Evident penetrations between the contact pairs should be avoided in the FE analyses. Two different sets of boundary conditions were used in the 2D axisymmetric FE model:[26]

Set 1: Radial displacement $U_y = 0$ was applied at the rivet axis and the far ends of the sheets. A vertical displacement $U_x = 0$ was applied at the two corner points of the outer side edge. One rigid set supported the rivet bottom and one rigid pusher was used to squeeze the rivet driven head;

Set 2: A third rigid body was introduced to support the external surface of the outer sheet on the basis of the boundary conditions in set 1, as shown in Fig. 6.6.

The outer sheet surface did not touch the bottom rigid set during the riveting process if the finite element model used the boundary conditions in set 1, which was only an idealized case. To more accurately simulate actual testing conditions and to improve set 1, the joint outer sheet touched the third rigid body located at the joint bottom during the riveting process in set 2.
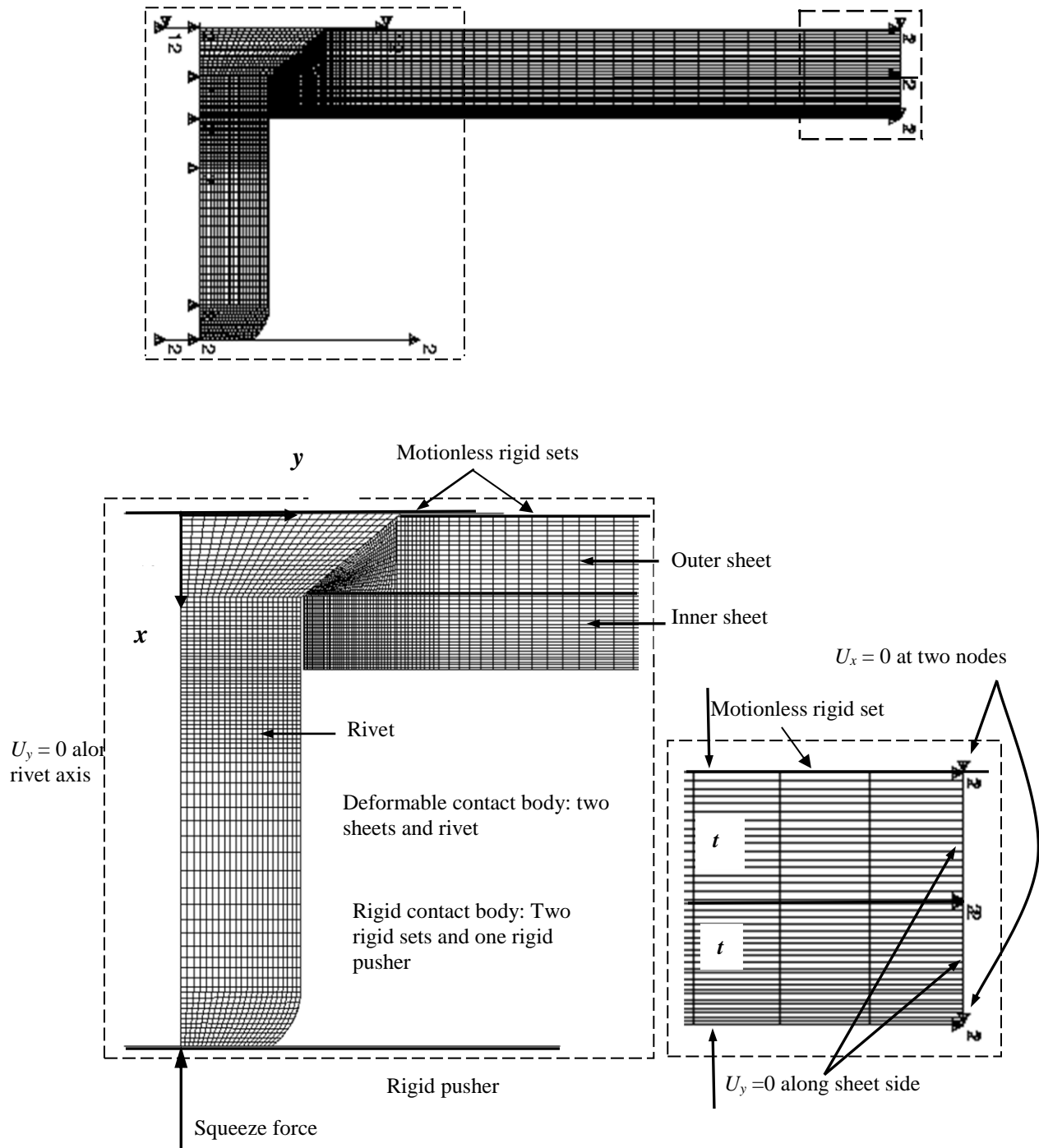
Fig. 6.6 Schematic diagram of the 2D axisymmetric finite element model with three deformable contact bodies, three rigid contact bodies, and the FE mesh and boundary conditions of Set 2 for the simulation of a lap joint.

Results and summary

Very little difference was found for the rivet deformations obtained from the numerical model using the displacement boundary conditions from Sets 1 and 2. Variations in the rivet driven head compressive displacement versus the squeeze force during the riveting process are presented in Fig. 6.7. It can be seen from this figure that the experimental results and the finite element predictions agreed very well. The rivet diameter deformation ratio of $\frac{D_{max}}{D}$ was 1.70 for both the experimental and numerical results. Fig. 6.8 shows the unriveted and riveted specimens, as well as the simulated rivet deformation.
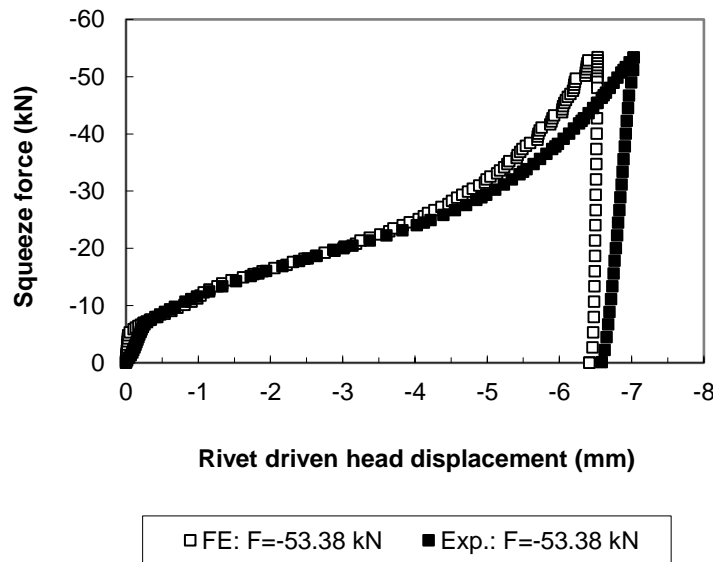
Fig. 6.7 Comparison of the rivet driven head displacement during the entire riveting period using the 53.38 kN rivet squeeze force determined by the experimental test and finite element method using the displacement boundary conditions of Set 1 or Set 2.
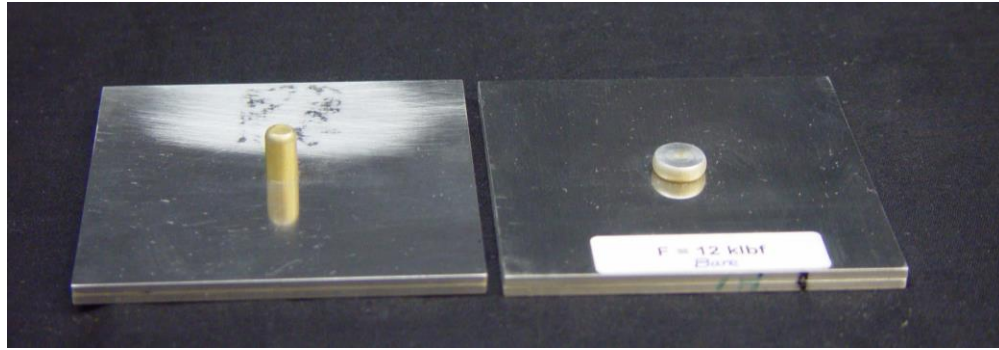
(a) Photographs of joint before riveting and after riveting using the 53.38 kN squeeze force
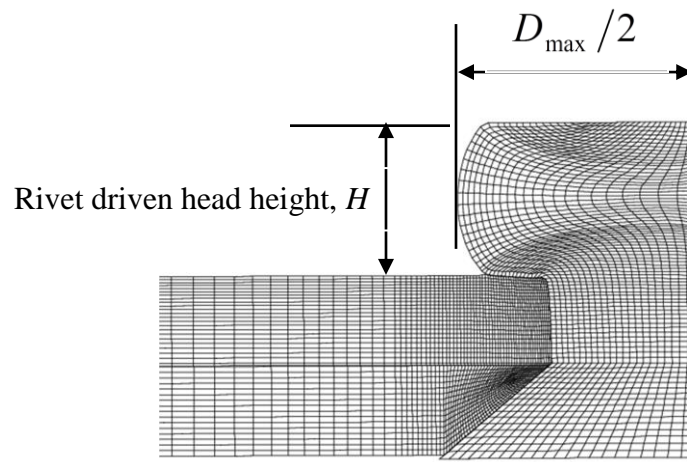
(b) FE prediction of rivet driven head shape riveted at the 53.38 kN squeeze force

Fig. 6.8 Rivet driven head shape obtained from the experiment and the FE analysis.

Comparisons of the strain variations obtained from the experimental tests and FE analyses for the radial and hoop directions are presented in Figs. 6.9 and 6.10, respectively. As can be seen from these figures, during the riveting process compressive strains were present in the radial direction while tensile strains were present in the hoop/tangential direction. Comparisons between the strain variation trends show good agreement between the FEM and experimental results for all the strain pairs except for a small portion during the entire riveting period. The numerical simulation resulted in excellent predictions for the hoop strain but was less accurate for the radial strain. Set 2 boundary conditions gave more accurate results than the boundary condition in set 1. A total of six contact bodies were used in set 2 while five

contact bodies were used in set 1. The three rigid contact bodies were two rigid sets and one rigid pusher, while the three deformable contact bodies were the two sheets and one rivet. From the experimental point of view, the boundary conditions of set 2 were more representative than that of set 1.
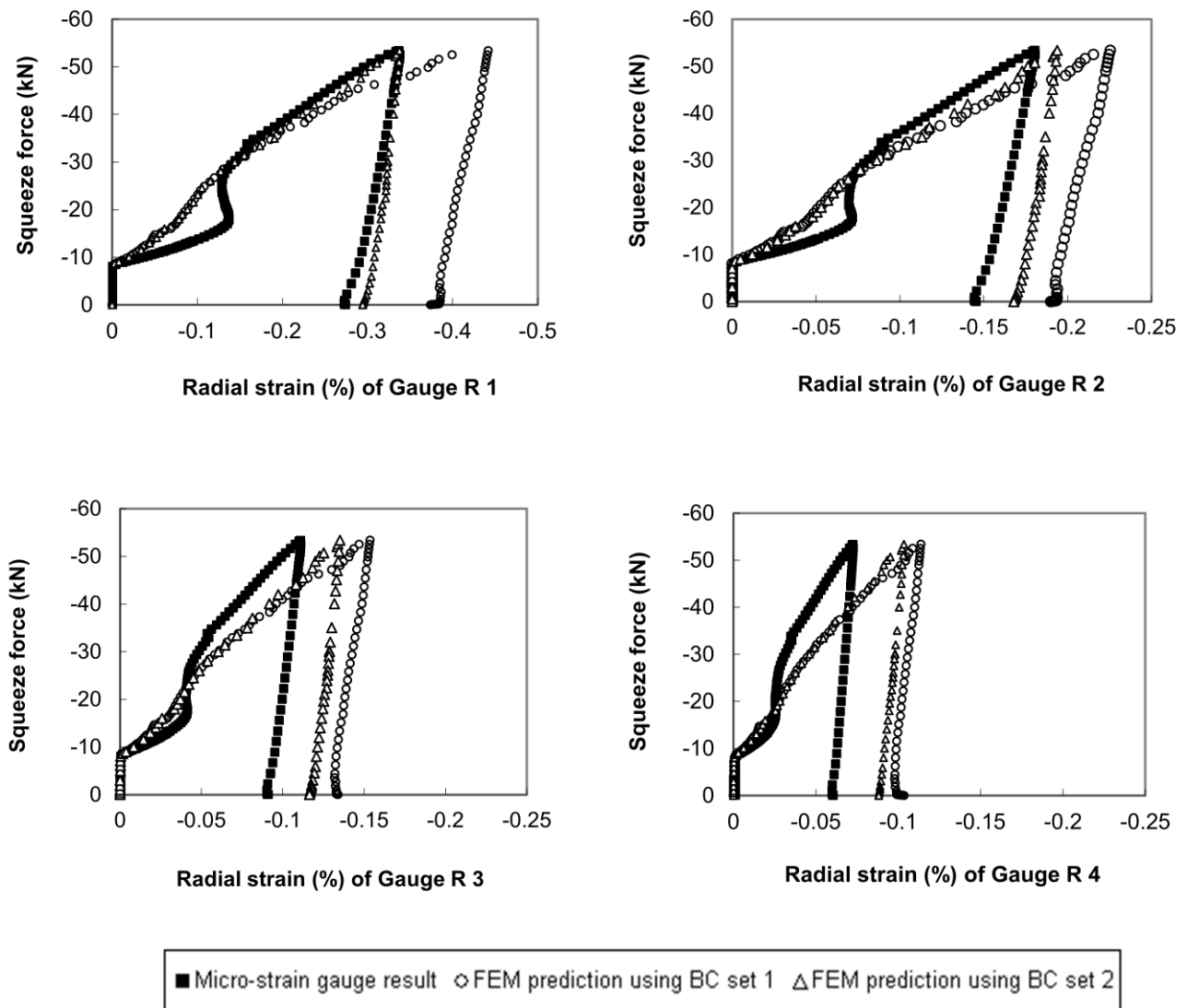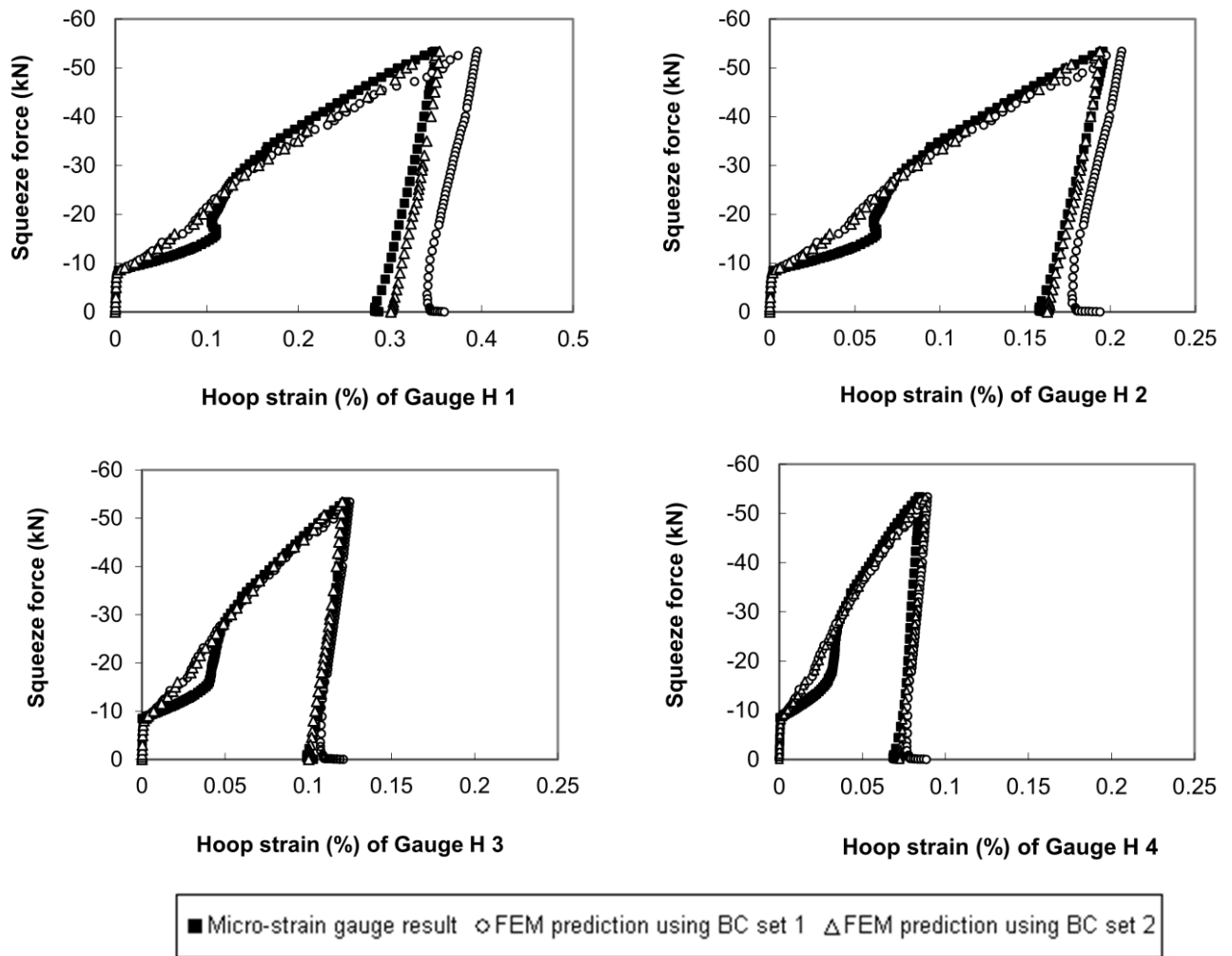

Fig. 6.9 Comparison of the radial strain variations in gauges R1 to R4 on the inner sheet surface during the riveting process under the 53.38 kN squeeze force obtained from micro-strain gauge and 2D FE results.

Fig. 6.10 Comparison of the hoop strain variations in gauges H1 to H4 on the inner sheet surface during the riveting process under the 53.38 kN squeeze force obtained from micro-strain gauge and 2D FE results.

Comparisons between the strain distributions in the radial, hoop and clamping directions from the neutron diffraction technique and the FE model, using the boundary conditions of set 2, are presented in Figs. 6.11 and 6.12 for the outer sheet and the inner sheet, respectively. Upper and lower bounds for the strain values obtained from the neutron diffraction technique are also presented in these two figures. The depths, x direction, of the data point for ε_x (or ε_y) and ε_z inside the outer sheet were different due to the measurement adjustment of the gauge centre. Reasonable agreement was achieved between the neutron diffraction results and the numerical predictions. The reasons of the discrepancy in the results are briefly explained elsewhere.[25, 26] These comparisons show that the 2D axisymmetric FE model can be
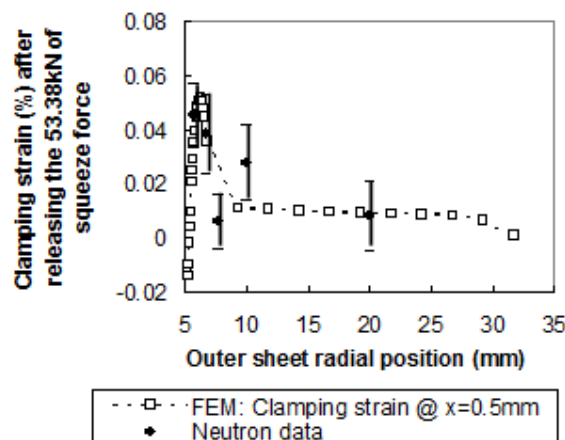
effectively used to simulate the riveting process. Therefore the residual stresses could be obtained using the developed 2D FE model for any location within a lap joint or at any loading.
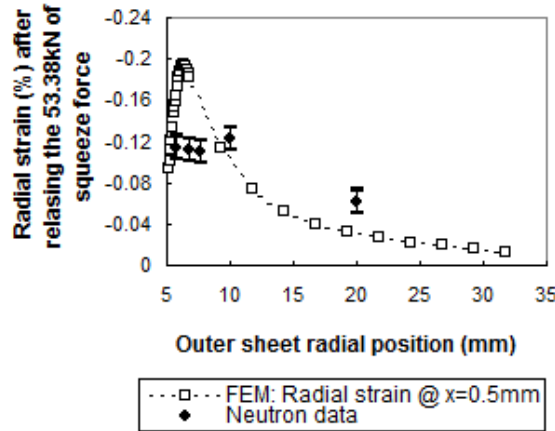
(a) Radial strain
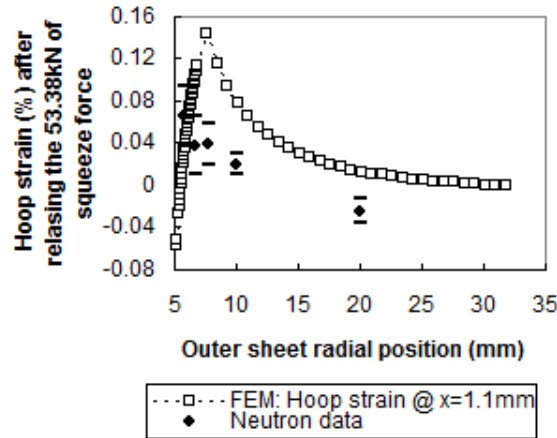
(b) Hoop strain

(c) Clamping strain

Fig. 6.11 Comparison of residual strains in the outer sheet along the radial position predicted by the numerical method and neutron diffraction after unloading the 53.38 kN squeeze force.
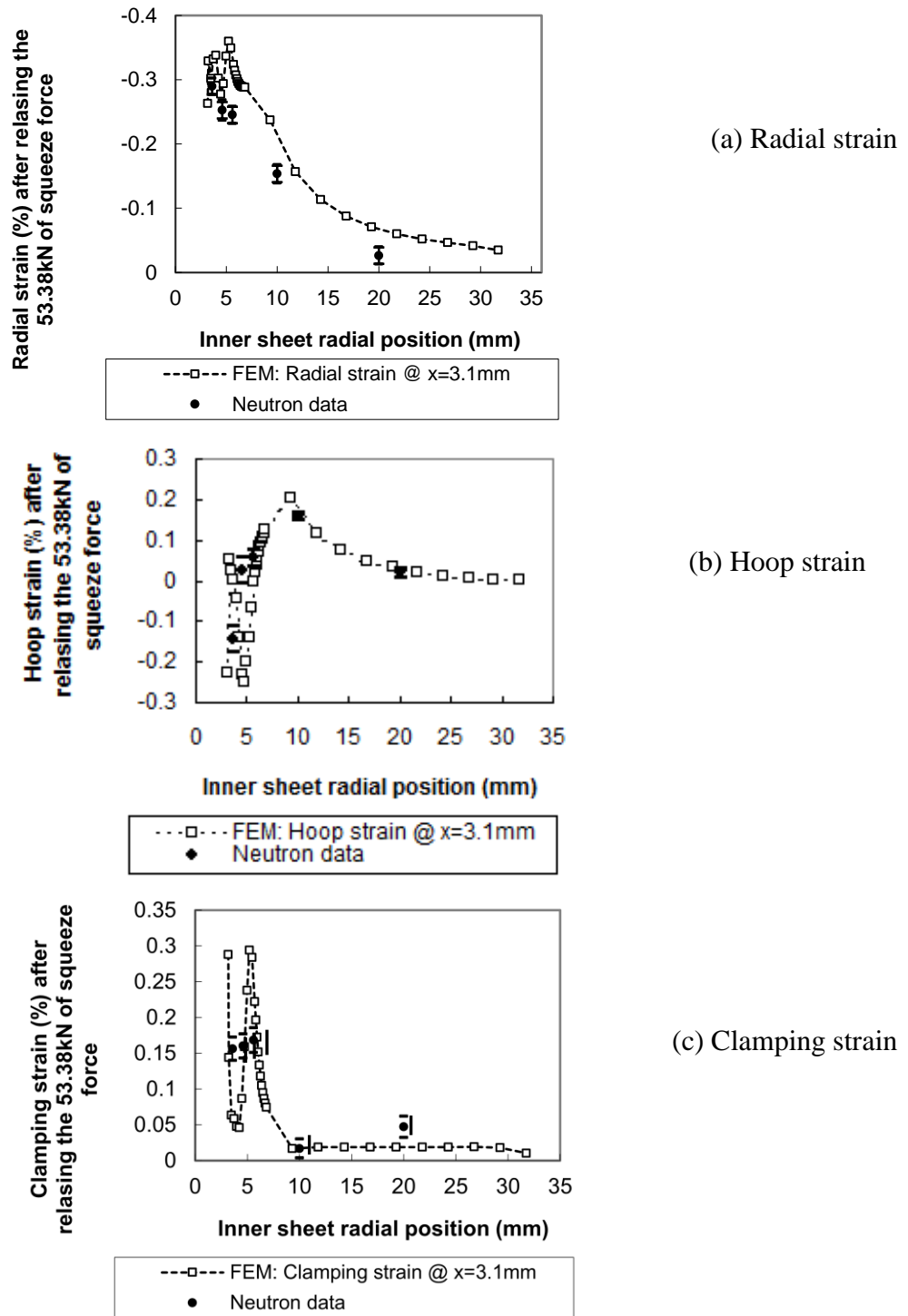
(a) Radial strain

(b) Hoop strain

(c) Clamping strain

Fig. 6.12 Comparison of residual strains in the inner sheet along the radial position predicted by the numerical method and neutron diffraction after unloading the 53.38 kN squeeze force.

Large squeeze forces induced big rivet driven head deformations. The final rivet deformations obtained from both experimental and finite element methods after releasing the squeeze force are plotted in Fig. 6.13. The maximum relative error of the finite element predictions to the experimental results was around −0.5% for the ratio of the rivet shank diameter deformation D_{max}/D and 1.5% for the rivet head height H. Good agreement was achieved for the rivet driven head deformations between the experimental and finite element results.
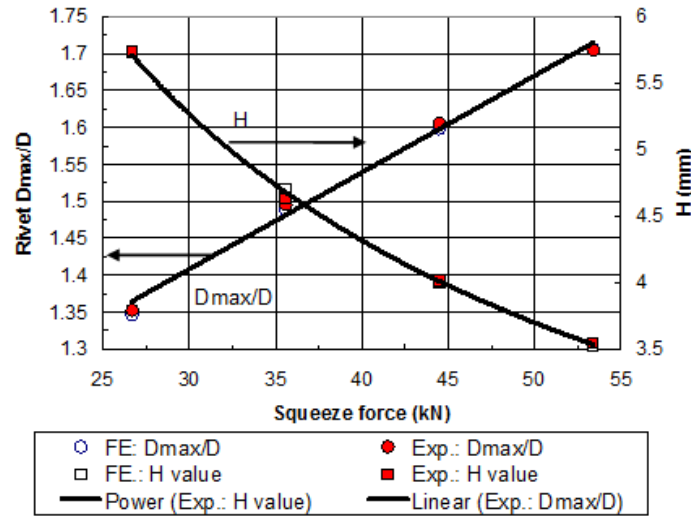
Fig. 6.13 Comparison of rivet driven head deformation and the rivet driven head height H obtained from experimental and FE results under four different rivet squeeze forces.

Interference is an important parameter to evaluate the quality of the joint riveting process,[4, 5, 7-9, 16] which should be a non-zero positive value and induced by a large rivet plastic deformation. A tight connection between fastener and sheets can be achieved if a large interference is introduced during riveting. The non-linear radial displacement and the interference distribution profiles at the sheet hole edge obtained from the numerical simulation results are shown in Fig. 6.14. In this figure, interference is defined to be the sheet hole radial expansion strain. The maximum and minimum interference at the sheet hole edge was around 5.1% and 0.27% respectively, after releasing the 53.38 kN squeeze force. A large interference is achieved only in the inner sheet. Variation in the outer sheet interference is not sensitive to the applied squeeze force and is small when the squeeze force is up to 53.38 kN. Results show that the connection between the outer sheet and rivet was weaker than that with the inner sheet.

Full-field residual contours of Von Mises stress, radial stress, hoop/tangential stress, and hoop strain after riveting are presented elsewhere.[25, 26] Full-field contours show that the magnitude of the compressive residual stress increased with the squeeze force, and a large expansion of

the rivet against the sheet hole interface was achieved. Non-linear distributions for the radial stress in both the radial and sheet thickness directions were observed.
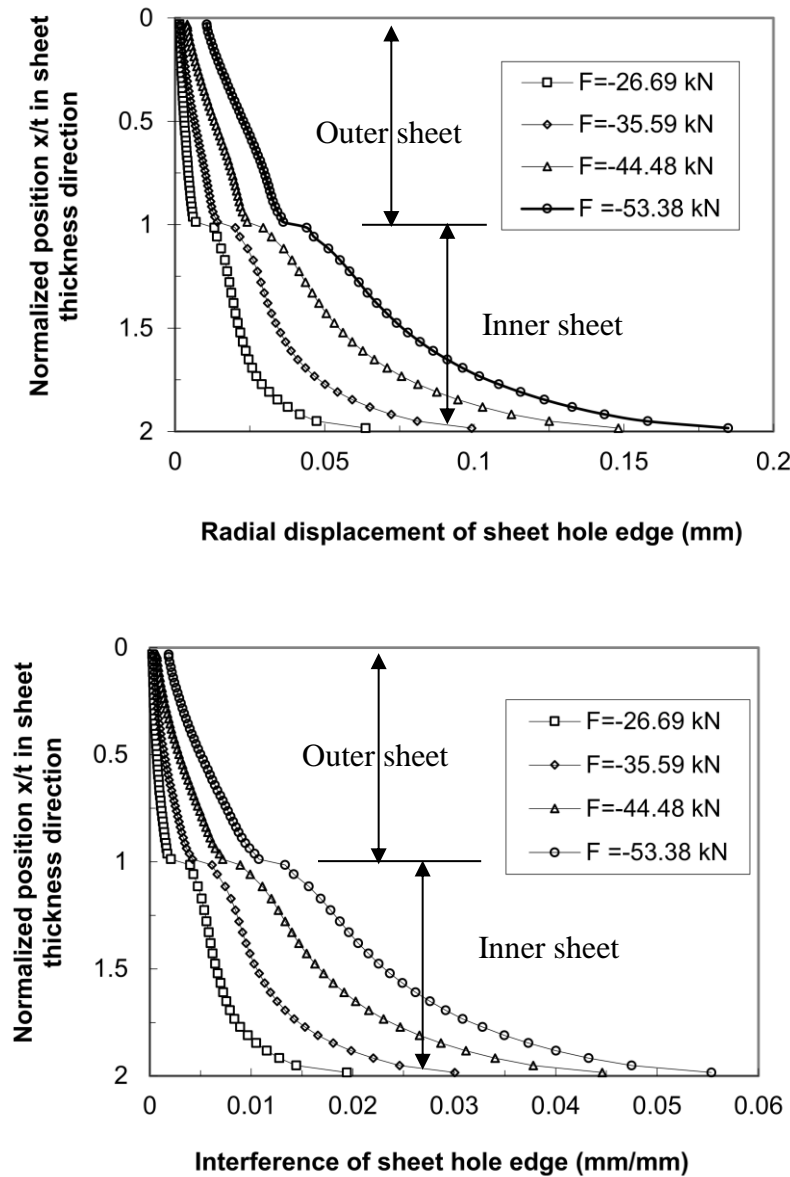
Fig. 6.14 Variations in the interference at the hole edge through the joint sheet thickness.

6.5.2   Case study 2: stress condition in three-row countersunk riveted lap joints

Because three-row countersunk riveted lap joints are typically used for fuselage structures, the study of the stress condition in this kind of lap joint is of practical importance. Secondary bending is generated due to the eccentricity of the load path when the riveted lap joints are loaded in tension. The residual stress/strain field, joint configuration, and secondary bending make the stresses/strains in the hole vicinity very different from the remote tensile stress/strain

conditions. The main objective of this case study was to demonstrate that 3D FE methods with proper settings can handle this complicated stress analysis. This study covered the entire loading sequence from the riveting process to the joint remote tensile loading stage.[27, 28]

Experimental aspect

Three joint specimens were tested,[28] which consisted of two bare 1.60 mm thick aluminum 2024-T3 alloy bare sheets, riveted with three aluminum 2117-T4 alloy countersunk-type MS20426AD5-6 rivets. The material properties used for the sheets were $E = 72.4$ GPa, $v = 0.33$, and $\sigma_y = 310$ MPa (initial yield stress), whereas the ones used for the 2117-T4 aluminum alloy rivet[15] were $E = 71.7$ GPa, $v = 0.33$, and $\sigma_y = 172$ MPa. Referring to Eq. [6.1], the hardening parameters used for the sheets were: $C = 676$ MPa and $m = 0.14$ when $\varepsilon_y < \varepsilon_{true} \le 0.02$ (ε_y was the initial yield strain), $C = 745$ MPa and $m = 0.164$ when $0.02 < \varepsilon_{true} \le 0.10$, and the slope of the linear hardening curve was 1.034 GPa when $\varepsilon_{true} > 0.10$. The hardening parameters[15] used for the rivet were the same as in case study 1. Three rivet squeeze forces of 10 kN, 14 kN, and 18 kN were used to install the rivets in each joint. After riveting, the lap joints were loaded in tension to a maximum remote stress of 98.6 MPa. Joint configuration and dimensions are given in Fig. 6.15 and Table 6.2, respectively. The mean radius clearance between the rivet and hole was 0.06 mm. Tabs with dimensions of 50×25.4×1.60 mm were bonded to the ends of each joint, to eliminate the initial secondary bending moment that would be induced when the joints were installed in the load frame. Micro-strain gauges, MM EA-13-031DE-350 and MM EA-13-031EC-350, were used to capture strain variations during the riveting process and then during the joint tensile loading stage. Details of the strain gauge mounting sequence, and positions on the joints can be found elsewhere.[28, 29]

Lap joints were riveted and then loaded in tension using a 250 kN MTS Load Frame with serial number 455 and model number 311.11. A small constant load ramp of 111.2 N/second was chosen for all the rivet installations.[30] Three rivets were installed one at a time, starting from the middle rivet. To keep the riveting condition the same, each coupon was held firmly to a mobile heavy metal plate. Gauges were reset to zero before the next riveting process to avoid any potential disturbances to both gauge and coupon. After riveting, the joints were loaded in tension to a maximum remote stress of 98.6 MPa. The tensile loading rate was 0.5 mm/minute. These strain data and rivet driven head deformations were used to validate the numerical predictions.
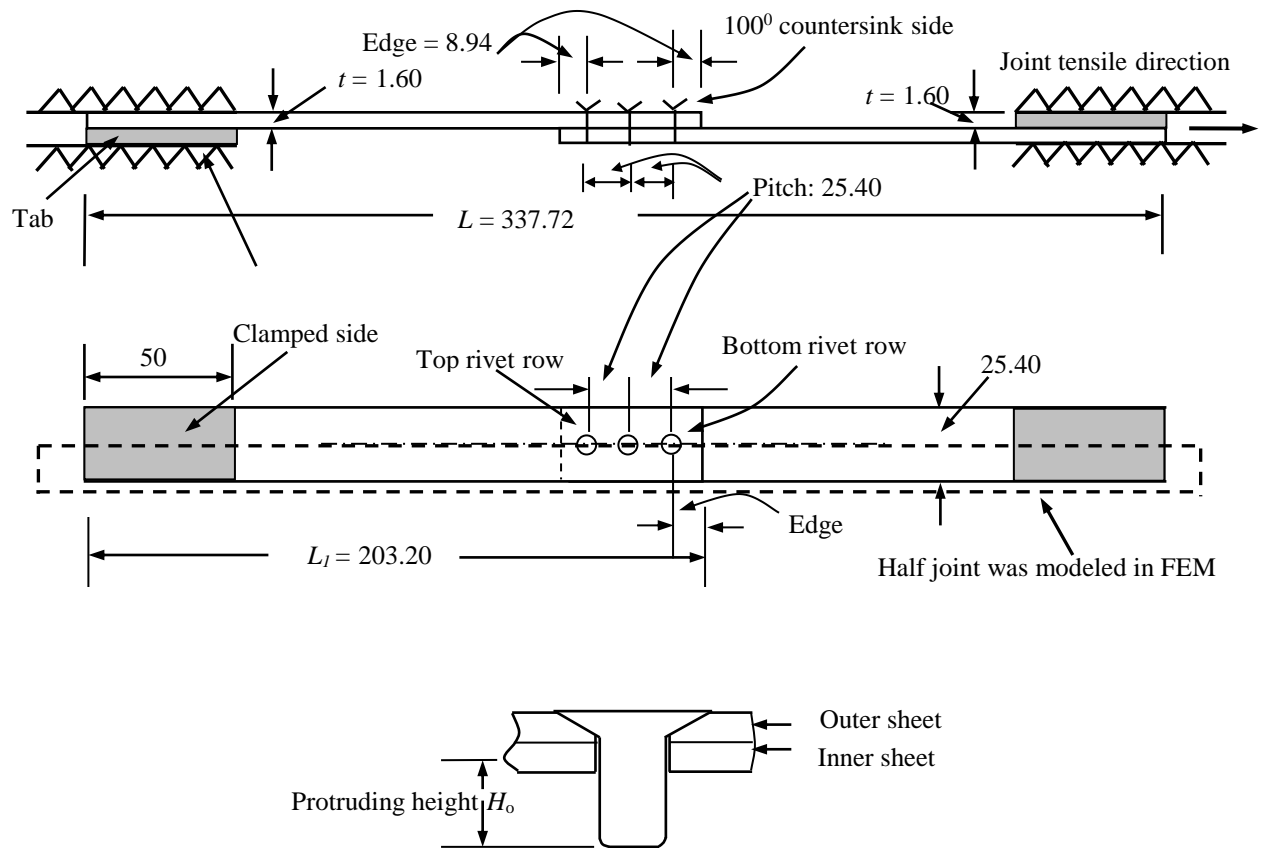
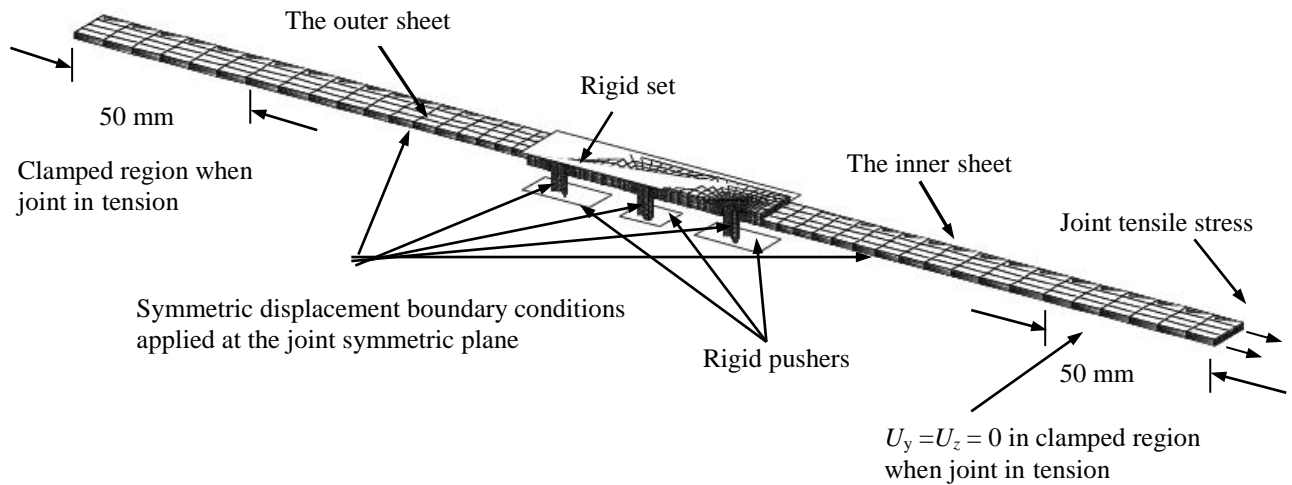**Fig. 6.15** Diagram of the lap joint with three countersunk rivets (dimensions: mm).

Table 6.2 Joint dimensions (mm) based on optical measurements of the three specimens.

Sheet dimensions	Distance between the panel side edge and the nearby hole centre	Mean inner sheet hole diameter, D_{hole}	Mean rivet protruding height H_o	Rivet shank diameter, D
203.2×25.4×1.60	8.94	4.09	6.06	3.97

Three-dimensional FE modeling

Owing to the joint symmetry, only half of the joint, as shown in Fig. 6.15, was modeled. Symmetric boundary conditions were applied to the joint centre plane along the longitudinal

x direction. The FE model was generated in accordance with the experimental joints using the FE software packages MSC.Patran (pre- and post-processor) version 2004r2 and MSC.Marc (solver) version 2001. A total of 12 362 nodes and 9096 8-node three-dimensional reduced integration brick elements (type 117) were used, as shown in Fig. 6.16. Element type 117 is an 8-node isoparametric arbitrary hexahedral for general three-dimensional applications using reduced integration. This element uses an assumed strain formulation written in natural coordinates that insures good representation of the shear strains in the element and is preferred over high-order elements when used in a contact analysis.[31]

The outer sheet

Rigid set

50 mm

Clamped region when joint in tension

The inner sheet

Joint tensile stress

Symmetric displacement boundary conditions applied at the joint symmetric plane

Rigid pushers

50 mm

$U_y = U_z = 0$ in clamped region when joint in tension

(a) Three-dimensional FE model

The outer sheet

The inner sheet

Top row rivet

The symmetric plane

Lower row rivet
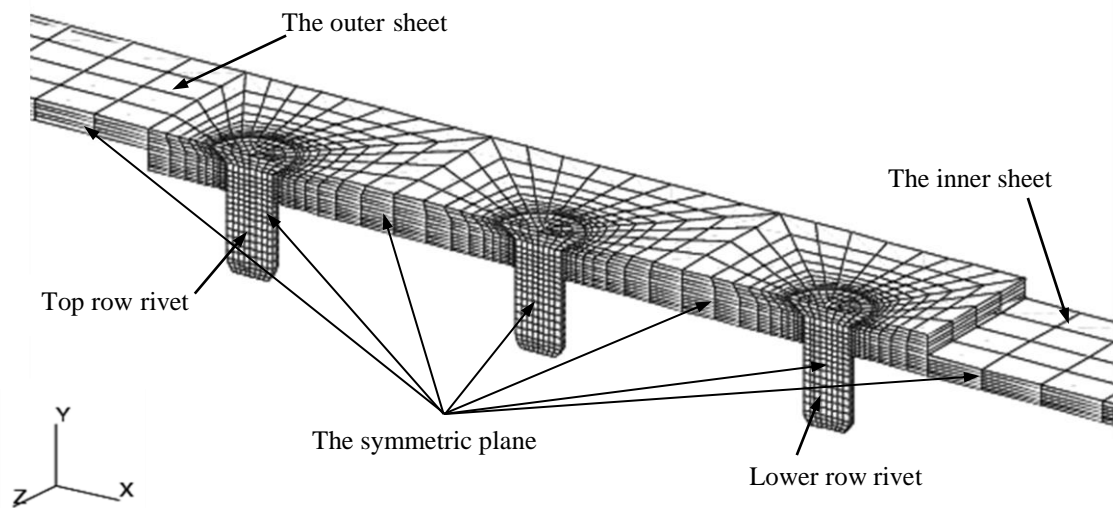
(b) Over lap region after removal of four rigid bodies

Fig. 6.16 The 3D FE model for the lap joints meshed using a total of 9,096 8-node reduced integration brick elements and 12,362 nodes.

Five deformable contact bodies, two sheets and three rivets, four rigid contact bodies, three pushers and one rigid set, were defined in the FE model. The rigid set contacted the joint bottom surface. Three rigid pushers were used to squeeze the three rivet driven heads. Specific contact pairs for both surface-to-surface and point-to-point were not needed since the current finite element software package could handle this particular contact situation if it occurred. A friction coefficient of 0.2 was used in the Coulomb model for all contact surfaces. A force-controlled riveting method was used in this numerical study. The same squeeze force was used to install all three rivets in one joint.[16, 17]

The multiple load steps, with their specific boundary conditions, were defined in a single loading sequence. Load step 1 applied the squeeze force to the centre pusher to squeeze the centre rivet; load step 2 released the squeeze force back to 0; load step 3 applied the squeeze force to the top rivet pusher, which squeezed the top rivet; load step 4 released the squeeze force back to 0; load step 5 applied the squeeze force to the lower rivet pusher, which squeezed the lower rivet; load step 6 released the squeeze force back to 0; and load step 7 applied the in-plane loading to the joint, up to a maximum stress of 98.6 MPa. In the final load step, the three deformable bodies contacted each other while the rigid bodies were deactivated. Details of displacement boundary conditions and contact pairs used in each step can be found elsewhere.[28, 29]

Comparisons of the experimental and FE results

Rivet driven head deformations are summarized in Table 6.3 and shown in Figs. 6.17 and 6.18. The relative difference between the experimental and numerical results for the driven head deformation ratio D_{max}/D was within 2%. During the riveting process, micro-strain gauges 1 to 3 were used to capture the hoop strains of the three holes, and gauge 4 was used to capture radial strains at one hole. Their positions are shown in Fig. 6.17. Due to the distance between the rivets, the riveting process did not influence the adjacent holes.[16, 17] To have a clear comparison of hoop strain variation during the riveting process, the experimental average hoop strains for gauges 1 to 3 ($\varepsilon_{avg} = \dfrac{\varepsilon_{G1} + \varepsilon_{G2} + \varepsilon_{G3}}{3}$) were used because they were located at similar positions relative to their neighboring holes. Comparisons of the average hoop strain from gauges 1 to 3 and the radial strain from gauge 4, during the riveting process, are presented in Fig. 6.19(a). Quantitative strain comparisons, during the tensile loading stage, were further carried out to validate the numerical results. To be consistent, the average residual strain, ε_{avg}, were again used as the initial value for the gauges 1 to 3 during the tensile loading stage. Comparisons of the strain variations during the joint tensile loading stage are presented in Fig. 6.19(b). Discussions on these comparisons can be found elsewhere.[28] Generally, good agreement was achieved for both the rivet driven head deformation and strain variations between the experimental and FE results. It could be drawn from these comparisons

that the residual stress, induced by the riveting process and stress conditions during the joint tensile loading stage, could be analyzed using the current numerical model with reasonable accuracy.

Table 6.3 Rivet deformations of D_{max}/D obtained from the experimental and the 3D finite element analysis (FEA) results.
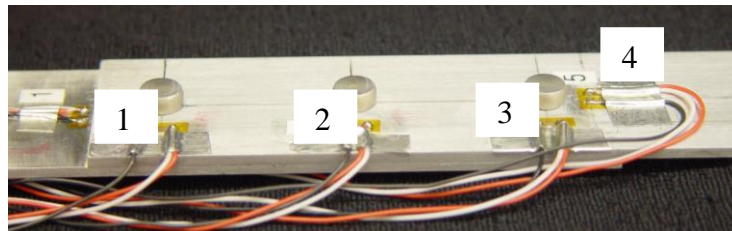
Rivet squeeze force	Test D_{max}/D	FEA D_{max}/D
10 kN	1.31	1.32
14 kN	1.50	1.52
18 kN	1.63	1.66
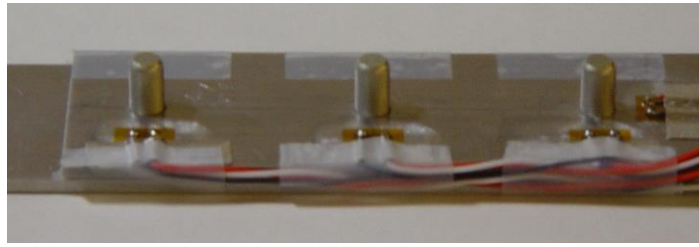
(a) Before riveting
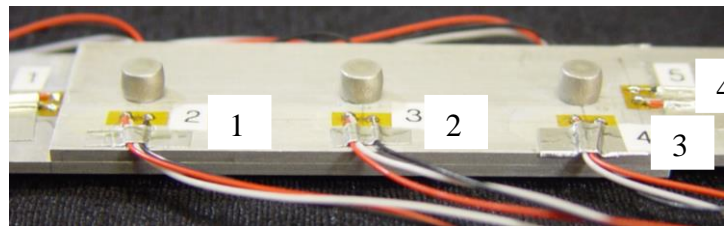
(b) Riveted by rivet squeeze force (RSF) = 10 kN
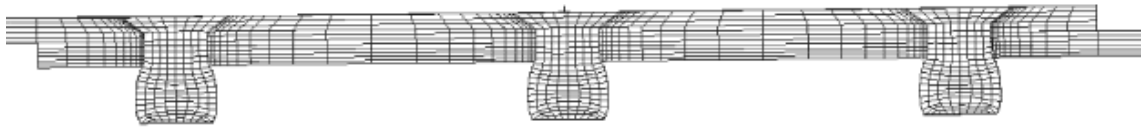

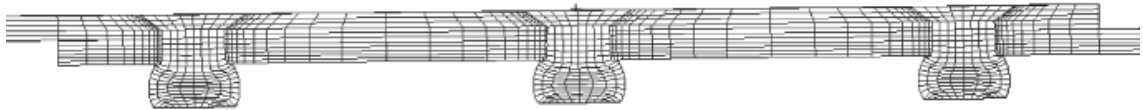(c) Riveted by rivet squeeze force (RSF) = 14 kN
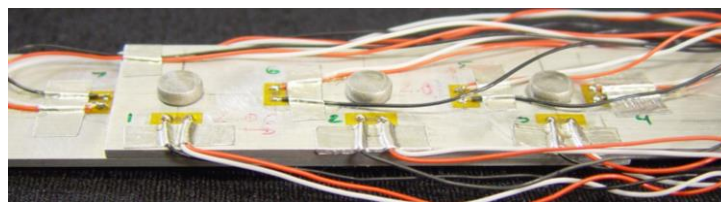
(d) Riveted by rivet squeeze force (RSF) = 18 kN

Fig. 6.17 Photos of the MS20426AD5-6 rivet driven head deformations in the lap joints, after the riveting process, using different rivet squeeze forces.

(a) Joint was loaded in tension to 98.6 MPa after the riveting process using the 10 kN squeeze force
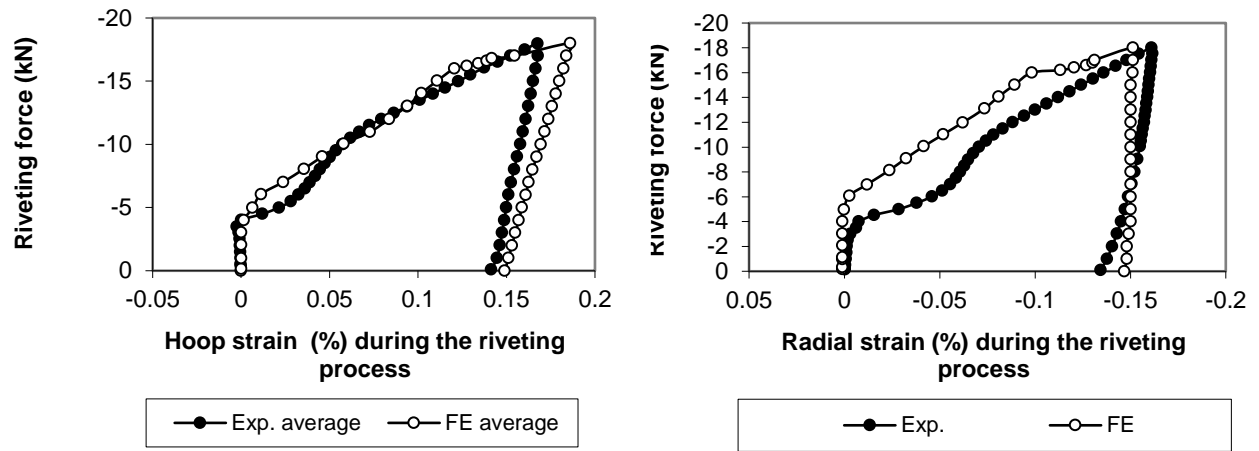

(b) Joint was loaded in tension to 98.6 MPa after the riveting process using the 14 kN squeeze force
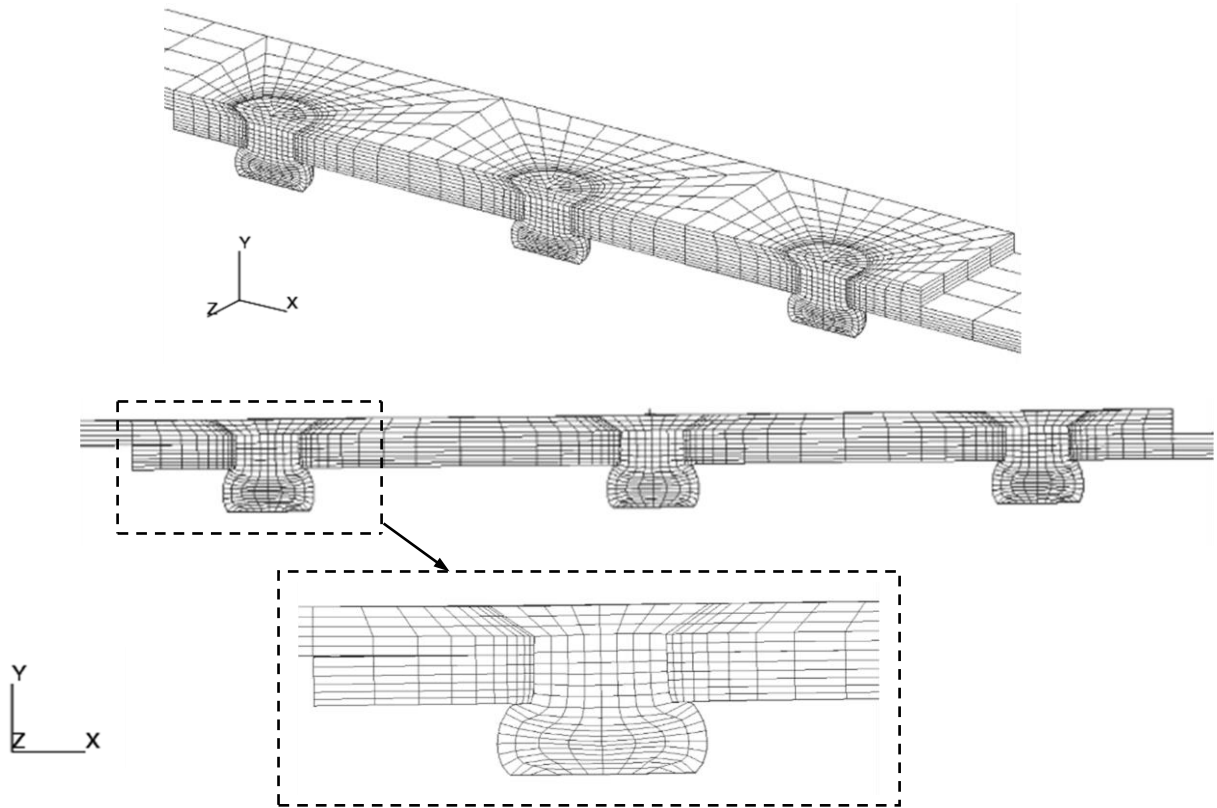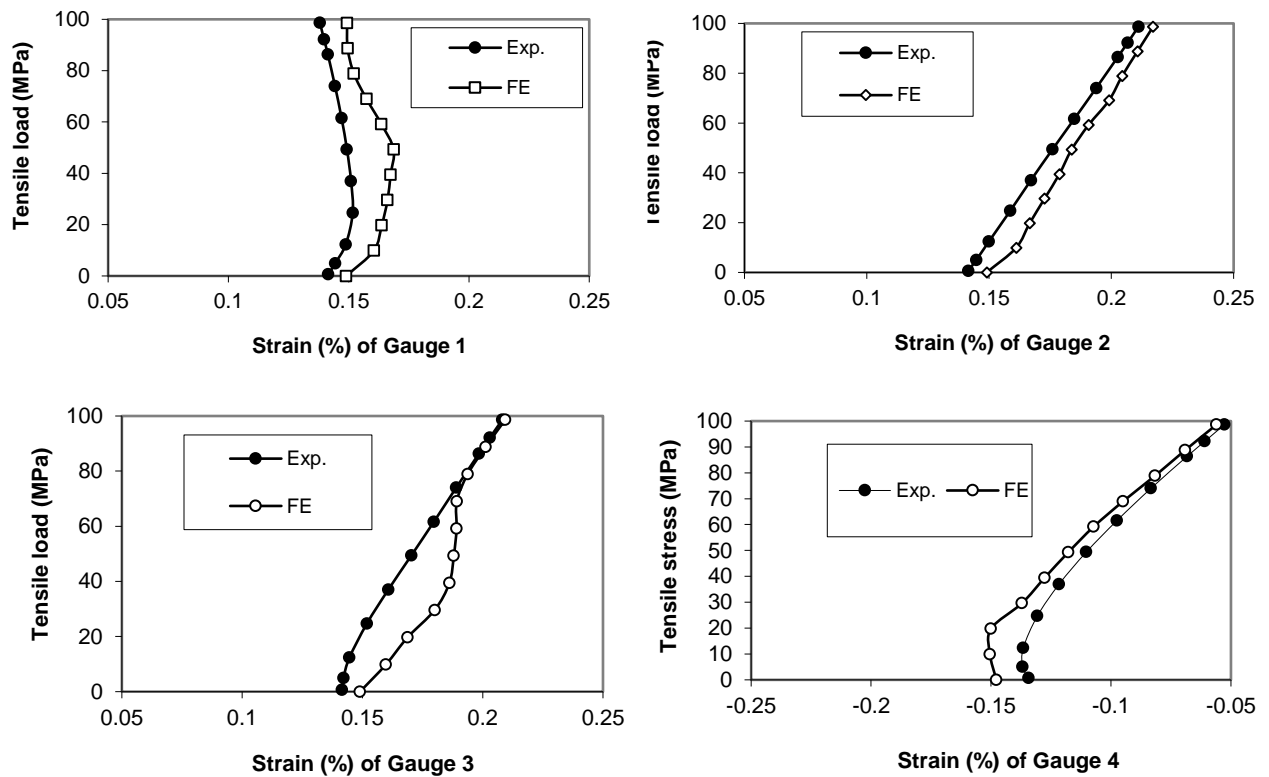

(c) Joint was loaded in tension to 98.6 MPa after the riveting process using the 18 kN squeeze force

Fig. 6.18 Lap joint deformations during the tensile loading stage, after the riveting process. No penetrations occurred.

(a) Strain variations during the riveting process using the 18 kN squeeze force

(b) Strain variations during the tensile loading stage after releasing the 18 kN squeeze force

Fig. 6.19 Comparison of the strain variations in gauges 1 to 4 joints during the (a) riveting process and (b) tensile loading stage.

Parametric study using the validated 3D FE model

Two more factors were numerically studied:[29] (i) the clearance between the sheet/rivet interface and (ii) the friction coefficient. The different tasks are listed in Table 6.4. It can be seen that two additional clearances of 0.12 mm and 0.18 mm were considered along with the previous value of 0.06 mm, and that two additional friction coefficients of 0.4 and 0.6 were considered besides the previous value of 0.2 in the Coulomb friction model.

**Table 6.4** Tasks carried out in the case study 2 for the three-row riveted lap joints.

| **Task 1** Validation of 3D FE model using corresponding test data: the friction coefficient was 0.2 used in the FE analysis			
Condition	Mean clearance	Rivet squeeze force	Notes
Clearance 1	0.06 mm	10 kN	Both Experimental and FE carried out.
		14 kN	
		18 kN	
Task 2 Parametric study using the validated 3D FE model			
Task 2.1 Effect of clearance on the stress condition			
Condition	Mean clearance	Rivet squeeze force	Notes
Clearance 2	0.12 mm	18 kN	3D FE only using the 0.2 friction coefficient
Clearance 3	0.18 mm	18 kN	
Task 2.2 Effect of friction coefficient on the stress condition			
Condition	Friction coefficient	Rivet squeeze force	Notes
Coefficient 2	0.4	18 kN	3D FE only under the Clearance 1 of 0.06 mm condition
Coefficient 3	0.6	18 kN	

Results and summary

The magnitude of the hoop stress in the top fastener hole vicinity along a transverse path on the outer sheet faying surface, were used as an indicator of the effects of rivet squeeze force, clearance, and friction coefficient on the stress condition in the riveted lap joints during the joint tensile loading stage. This path was selected because the section in the top rivet row area of the outer sheet is relatively weak and usually fails first.

The hoop stress variations along the prescribed path, considering the influence of the rivet squeeze force, are presented in Fig. 6.20. The following characteristics can be observed from

this figure: (i) large rivet squeeze force generates a large compressive hoop stress at the hole edge and (ii) nonlinear variations in the hoop stress occurred during the tensile loading stage. This figure shows that the residual stresses induced by the rivet squeeze force have considerable effect on the stress variations during the tensile loading stage. When the joint remote tensile stress was 98.6 MPa, the corresponding increments of the hoop stress magnitude was approximately 128%, 58%, and 50% using the three rivet squeeze forces, compared to the residual hoop stress at the hole edge induced by the 10 kN rivet squeeze force.
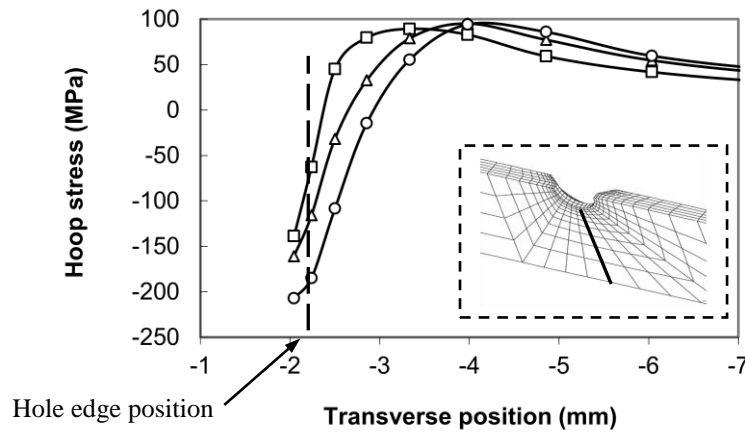
(a) Remote tensile stress of 0 MPa
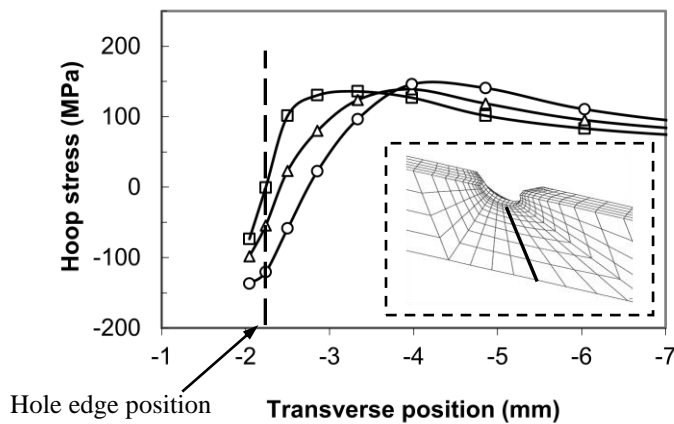
(b) Remote tensile stress of 49.3 MPa
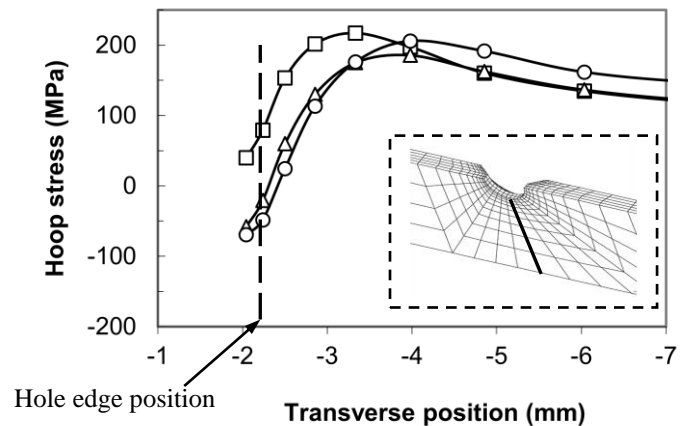
(c) Remote tensile stress of 98.6 MPa

Fig. 6.20 Hoop stress variations along the transverse path during the tensile loading stage, after releasing the three different RSF, □: 10 kN, Δ: 14 kN and O: 18 kN.

Provided that the joint was riveted using the 18 kN rivet squeeze force and, assuming a 0.2 friction coefficient, the effect of the clearance between the sheet/rivet interface on the hoop stress variations are shown in Fig. 6.21. Three different clearances of 0.06 mm, 0.12 mm, and 0.18 mm were studied. It can be seen from this figure that the clearance had a significant influence on the hoop stress in the hole vicinity. A small clearance led to large compressive hoop stresses in the hole vicinity and a large clearance resulted in tensile stresses in the hole vicinity. For clarity, hoop stress information in the hole vicinity is summarized in Table 6.5. When the clearance was changed from the 0.06 mm to 0.18 mm, it can be observed from this table that (i) the stress increment at the hole edge could be up to +349%, (ii) the increase in the maximum stress was as high as +24%, and (iii) the distance between the location of the maximum stress and the hole edge decreased from 1.94 mm to 1.28 mm, when the large clearance of the 0.18 mm was used. One clear finding is that the large clearance would significantly increase the hoop stress magnitude at the hole edge, which strongly suggested that the fatigue strength of the lap joints would be seriously reduced, which is consistent with available experimental results.[32]
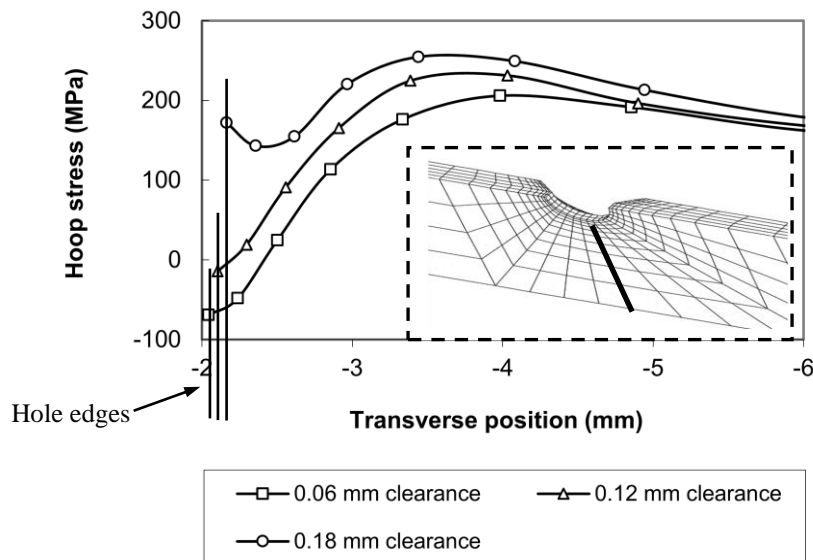

Fig. 6.21 Effects of the clearance fit on the hoop stress variations along the transverse path when the joints in tension to 98.6 MPa after releasing the 18 kN squeeze force.

Table 6.5 Increment (%) in the hoop (longitudinal) stress as compared to the joint with the 0.06 mm clearance.

Condition	During the tensile loading stage				
Clearance	Stress at the hole edge	Increment at the hole edge	Maximum stress in the hole vicinity	Distance to the hole edge	Increment of the maximum stress
0.06 mm	−69.2 MPa	0	205.9 MPa	1.94 mm	0
0.12 mm	−14.5 MPa	+79%	231.3 MPa	1.93 mm	+12%
0.18 mm	172 MPa	+349%	254.6 MPa	1.28 mm	+24%

When the 0.06 mm clearance joints are loaded in tension after releasing the 18 kN squeeze force, the effects of the friction coefficient on the hoop stress variations were examined and plotted in Fig. 6.22. Little difference was observed in the results for the three different friction coefficients used.
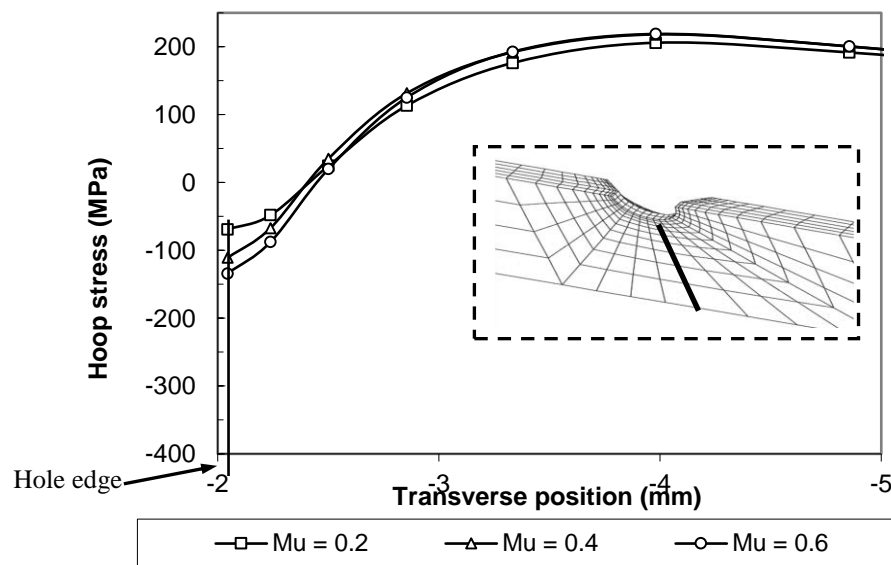

Fig. 6.22 Effects of the friction coefficient in the Coulomb model on the hoop stress variations along the transverse path when the joints were loaded to 98.6 MPa after releasing the 18 kN squeeze force.

The full-field stress distributions of the maximum principal stress can be found elsewhere.[29] The effect of rivet squeeze force is presented in Fig. 6.23. The maximum principal stress is of great importance in the study of crack nucleation during the tensile loading stage. These full-field stress contours show that large maximum principal stresses mainly occurred at the top rivet row hole region. A large rivet squeeze force moved the high stressed region away from the holes' edge vicinity. The largest maximum principal stress in the top rivet region increased with the increment in the clearance, which intersected the top fastener hole for both the 0.12 and 0.18 mm clearance fits. A large friction coefficient increased both the stress magnitude and high stress area in the top rivet hole region, however, its impact was less than that of the clearance. The large maximum principal stress distribution area and shape were consistent with the experimental fatigue testing results.[18] In the fatigue tests of non-corroded joints, cracks typically originate in the outer sheet heavily fretted area around the upper rivet hole a short distance away from the top rivet hole edge.[18]

It is possible to study the entire loading stages for the three-row countersunk riveted lap joints using 3D FE methods. The effect of rivet squeeze force, clearance, and friction coefficient on the stress/strain condition in the lap joints can be studied. The numerical results suggest that high strength lap joints could be fabricated using (i) a relatively large squeeze force to install rivets and (ii) a small clearance between the sheet hole and rivet shank interface.
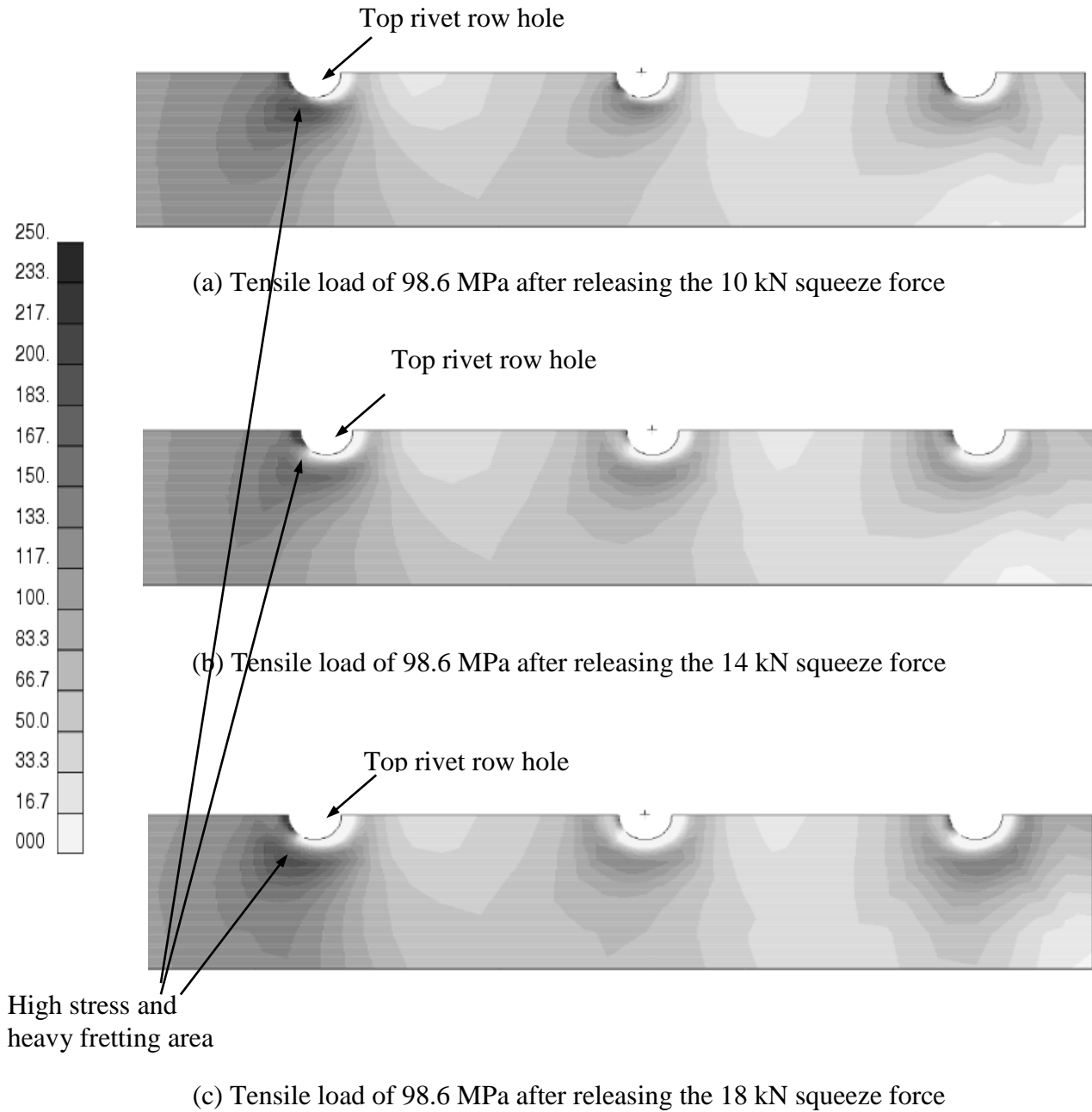
(a) Tensile load of 98.6 MPa after releasing the 10 kN squeeze force

(b) Tensile load of 98.6 MPa after releasing the 14 kN squeeze force

(c) Tensile load of 98.6 MPa after releasing the 18 kN squeeze force

Fig. 6.23 Maximum principal stress (MPa) on the outer sheet faying surface when the joints were loaded in tension by the 98.6 MPa stress. The 0.06 mm clearance and 0.2 friction coefficient were used in the FE analysis.

6.6 Concluding remarks

The weak location of the riveted lap joints is the outer sheet faying surface at the top row hole region. To improve the joint fatigue performance, a certain amount of interference and compressive residual stress/strain should be introduced to that region. However, current rivets and installation tools cannot achieve this target. It can be noticed from Fig. 6.14 that the higher level of interference is only present in the inner sheet and very little interference is generated in the outer sheet. Only the rivet driven head experiences a large compressive displacement, whereas the flush head or protruding head side does not experience enough compressive deformation. Two potential developments could be carried out to both the rivets and the corresponding rivet installation tools, to change this situation in the outer sheet. For a new generation of rivets aimed at introducing a certain amount of interference in both the inner and outer sheets, two aspects should be considered. These requirements could be that (i) both rivet heads could be driven heads so that both head sides would experience large compressive displacement during the rivet installation, and (ii) the induced interference magnitude could be controlled and its distribution through the joint thickness should be made relatively uniform. The corresponding rivet installation tools would therefore be designed to install these new rivets in metallic joints using one or two strokes to squeeze both rivet ends.

Acknowledgements

References

1   'Metallic Material and Elements for Aerospace Vehicle Structures'. MIL-HDBK-5H, Department of Defense, USA, Dec. 1998.

2   'Rivets, buck type, preparation for and installation of', *MIL-R-47196A-Notice 1*, Department of Defense, USA, 1986.

3   Niu, M.C.Y., 'Airframe Structural Design', Hong Kong, Hong Kong Conmilit Press Ltd., 1997.

4   Müller, R.P.G., 'An experimental and analytical investigation on the fatigue behavior of fuselage riveted lap joints', Ph.D. Thesis, Delft Univ. of Technology, Delft, The Netherlands, 1995.

5   Hazlehurst, L. and Woods, M., 'Automated rivet interference inspection system', *SAE International*, Warrendale, PA, 1994, paper 941842.

6   Donaldson, D.R. and Kenworthy, K.J., 'Fatigue design and test program for the American SST', *Aircraft Fatigue Design, Operational and Economics Aspects*, ed. J.Y. Mann and I.S. Milligan, Pergamon, Rushcutters Bay. 1972, 437-476.

7   Nepershin, R.I., Knigin, V.V., and Klimenov, V.V., 'Interferences and residual stresses in riveted joints", *Journal of machinery manufacture and reliability,* 1992, 5, 47-51.

8   Ryzhova, T.B., 'Estimation of the reliability of ultrasonic quality control of riveted joints with clearance', *Russian Journal of Nondestructive Testing*, 1994, 30, 418-421.

9   Ryzhova, T.B., 'Ultrasonic assessment of the radial clearance of riveted joints in aircraft structures', ICAS, Congress, 21st Melbourne, Australia, 1998, ICAS-98-R, 4, 1-7.

10   Fitzgerald, T.J. and Cohen, J.B., 'Residual stresses in and around rivets in clad aluminum alloy plates', *Materials Science and Engineering*, 1994, A188, 51-58.

11   Fung, C-P and Smart, J. 'An experimental and numerical analysis of riveted single lap joints', *J. of Aerospace Engineering*. 1994, 208 (2), 79-90.

12   Fung, C-P and Smart, J., 'Riveted single-lap joints. Part 1: A numerical parametric study', *J. of Aerospace Engineering*. 1997, 211 (1), 13-27.

13   Fawaz, S.A., Schijve, J., and de Koning, A.U. (1997), 'Fatigue crack growth in riveted joints', ICAF 97 – Fatigue in new and aging aircraft; Edinburgh, UK, 1997, 1, 553-574.

14   Ryan, L. and Monaghan, J., 'Failure mechanism of riveted joint in fibre metal laminates', *J. of Materials Processing Technology*, 2000, 103, 36-43

15   Szolwinski, M.P. and Farris, T.N., 'Linking riveting process parameters to the fatigue performance of riveted aircraft structures', *J. of Aircraft*, 2000, 37 (1), 130-137.

16   Trego, A. and Cope, D., 'Evaluation of damage tolerance analysis tools for lap joints', *AIAA Journal*, 2001, 39 (12), 2250-2254.

17   Bellinger, N.C., Komorowski, J.P., and Benak, T.J., 'Residual life prediction of corroded fuselage lap joints', *Int. J. of Fatigue*, 2001, 23, S349-S356.

18   Eastaugh, G.F., Straznicky, P.V., Krizan, D.V., Merati, A.A., Cook, J., 'Experimental study of the effects of corrosion on the fatigue durability and crack growth characteristics of longitudinal fuselage splices', *Proceedings of the Fourth DoD/FAA/NASA Aging Aircraft Conference*, St. Louis, MO. 15-18 May 2000.

19   Shi, G., Bellinger, N. and Xiong, Y., 'Three-dimensional nonlinear finite element modeling and analysis of riveted lap joints with corrosion pillowing', in Advances in computational engineering & science, v.II, ed. by Atluri, Satya N. and Brust, Frederick W., Tech Science Press, 2000, 1542-1547.

20   Mackerle, J., 'Finite element analysis of fastening and joining: A bibliography (1990-2002)', *Int. J. Pressure Vessels and Piping*, 2003, 80, 253-271.

21   Markiewicz, E., Langrand, B., Deleotombe, E., Drazetic, P., and Patronelli, L., 'Analysis of the riveting forming mechanisms', *Int. J. of Materials and Product Technology*, 1998, 13 (3-6), 123-145.

22   Langrand, B., Patronelli, L., Deleotombe, E., Markiewicz, E., Drazetic, P., 'An alternative numerical approach for full scale characterization for riveted joint design', *Aerospace Science and Technology*, 2002, 6, 343-345.

23   Li, G. and Shi, G., 'Residual stresses in riveted lap joints: a literature review', *LTR-SMPL-2002-0019*, Institute for Aerospace Research, NRC, Canada, 2002.

24   Li, G., Shi, G., 'Investigation of residual stress in riveted lap joints: Experimental study', *LTR-SMPL-2003-0099*, Institute for Aerospace Research, NRC, Canada, 2003.

25   Li, G. and Shi, G. 'Effect of the riveting process on the residual stress in fuselage lap joints', *Canadian Aeronautics and Space Journal*, 2004, 50 (2), 91-105.

26   Li, G., Shi, G., and Bellinger, N.C., 'Study of the residual strain in lap joints', *J. of Aircraft*, 2006, 43 (4), 1145-1151. **doi: 10.2514/1.18125**

27   Li, G., Shi, G., and Bellinger, N.C., 'Study of residual stress in single-row countersunk riveted lap joints', *J. of Aircraft*, 2006, 43 (3), 592-599.

28   Li, G., Shi, G., and Bellinger, N.C., 'Residual stress/strain in three-row countersunk, riveted lap joints', *J. of Aircraft*, 2007, 44 (4), 1275-1285. **doi: 10.2514/1.26748**

29   Li, G., Shi, G., and Bellinger, N.C., 'Numerical investigations of residual stress/strain conditions in lap joints with three-row countersunk rivets', *LTR-SMPL-2005-0045*, Institute for Aerospace Research, NRC, Canada, 2005.

30   Manual of MTS Load Frame, MTS systems Corporation, Box 24012, Minneapolis, Minnesota, USA 55424.

31   'MARC volume b: element library, Version K7', MARC analysis research corporation, USA, 1997.

32   'Fatigue rated fastener systems', edited by H.H. van der Linden, AGARD-R-721, North Atlantic Treaty Organization, 1985.